Towards Advancement of Continuous Fiber Composite Additive Manufacturing

Mallory Elizabeth Parker

A thesis
submitted in partial fulfillment of the
requirements for the degree of

Master of Science

University of Washington
2021

Committee:
Dwayne D. Arola
Eleftheria Roumeli
Navid Zobeiry

Program Authorized to Offer Degree*:*
Department of Materials Science and Engineering

University of Washington

Abstract

Towards Advancement of Continuous Fiber Composite Additive Manufacturing

Mallory Elizabeth Parker

Chair of the Supervisory Committee:

Associate Professor Dwayne Arola

Department of Materials Science and Engineering

Additive manufacturing (AM) of composite materials could play an unlimited role in the future of advanced engineering structures, particularly in aerospace. Specifically, fiber reinforced polymers (both thermoplastic and thermoset) offer incredible weight savings, with mechanical properties comparable to metal alloys. In turn, AM can provide design freedom and unlimited component complexity, qualities unavailable from traditional methods of manufacturing with composites. AM technologies, including fused deposition modelling in particular, have undergone rapid growth within industry and academia in the last several decades; new materials are being developed frequently. However, contributions from the printing process to the "printed" material properties are often overlooked, which are of critical importance to material reliability and aerospace applications.

In this effort the printability, material property variability and potential applications of a novel filament with high volume fraction of continuous fiber reinforcement were evaluated. The material is a new prototype system manufactured by Toray Industries, which consists of a 6k tow of continuous carbon fibers (CCF) within a polyphenylene sulfide (PPS) matrix. Filaments of CCF/PPS with fiber volume fractions between 30 and 50% nominal fiber volume fraction were printed, and results were compared with those achieved with commercially available composite material systems. Multiple design of experiments were performed to understand the effect of process parameters on the printed material quality, including nozzle Z-height, nozzle temperature, printing speed, and material flow rate.

Results showed that the printed quality in terms of dimensionality and roughness, matrix crystallinity, and fiber distribution within the printed filament were a function of the printing parameters. The prototype Toray filament achieved a tensile strength that exceeded 2 GPa, an elastic modulus of 155 GPa and a strain to failure of approximately 1.5%. Complimentary Weibull analyses were performed and combined with microstructural evaluation to assess the characteristics of filament failure in the unprinted and printed state. Although the strength of the CCF/PPS filament is the highest reported of any composite printed using the FDM process, there are several sources of defects that substantially reduce the strength of the printed material, by as much as 25%. Hence, further process optimization is needed for this CCF /PPS system and other continuous fiber composite materials to reach their full potential when used to manufacture components by FDM.

University of Washington
Graduate School

This is to certify that I have examined this copy of a master’s thesis by:

Mallory Elizabeth Parker

And have found it complete and satisfactory in all respects,

and that any and all revisions required by the

final examining committee have been made.

Committee Members:

____

Prof. Dwayne Arola, Chair

____

Prof. Eleftheria Roumeli

____

Prof. Navid Zobeiry

Date: _________________

Signature: ____________________________

Date: ________________________________

Table of Contents

LIST OF FIGURES

LIST OF TABLES

ACKNOWLEDGEMENTS

First and foremost, I would like to thank my family for their endless support. Their unwavering belief in my abilities makes me feel confident I can reach the stars. I would like to thank Dr. Dwayne Arola for guiding me throughout this time at the University of Washington. His encouragement and support have pushed me towards this exciting work and advancement of my career. I would also like to thank the additional members of my defense committee for their time and feedback; Dr. Eleftheria Roumeli and Dr. Navid Zobeiry. I also thank Dr. Ryosuke Matsuzaki for his input and guidance throughout our Toray Co. collaboration. Thank you to JCATI for providing funding to explore the exciting field of composite additive manufacturing. A special thank you to the students I have worked with and whose contribution to this thesis were invaluable, including Ngozi Ezeokeke, Amanda Inthavong, Esther Law, and Sarah Waddell. Finally, the research conducted for this thesis would not have been possible without members of the Arola group and the MSE department, thank you to all who helped me.

Chapter 1 – Introduction

A fairly ubiquitous principle within industries is added weight correlates to added cost. Within transportation industries, added weight is two-fold in increased fuel costs and supplemental design considerations. Recently, polymer composites have undergone an increase in applications across a number of manufacturing sectors, as they offer a lightweight alternative with tunable properties depending on the matrix/filler combination. To manufacturers' dismay, certification of a composite part for aircrafts and automobiles is extensive, but resulting parts are strong and durable. Trade-offs are weighed heavily and often there is a lack of capital in investigating novel material systems. Traditional composite manufacturing with prepreg, such as vacuum bagging and hand-layup, can have a steep upfront investment and resulting parts must have allowable tolerances due to a variety of defects that can occur during processing. To keep up with the demands of current industries, composite research must involve focus on manufacturing to create superior parts.

In pursing improved technologies, additive manufacturing (AM) is undergoing rapid and widespread advancements. 3D printers have become common desktop items, enabling endless production of small polymer and polymer composite objects. Research has begun to probe advancement of continuous fiber filaments for AM, but there is still much unknown about the fundamental influence of the printing process on composite properties. This thesis explores the printability of a promising high volume fraction composite filament and calls attention to future areas for process improvement.

1.1 Composite Manufacturing

The composite materials industry is a large economic force, and the push for increased product weight savings is driving innovation across all major manufacturing operations. Still, composites are inherently complex systems, as multiple discrete components (usually a matrix embedded with a reinforcement) work in concert. Composites can be defined by the filler type, which ranges from particles to continuous fiber-reinforcements. In the present study, polymer composites with continuous fiber reinforcement are of interest. Common fiber reinforcements such as carbon fibers, aramid (Kevlar) fibers, and glass fibers can enhance the tensile properties to rival those of some metal alloys (Hsissou, et al., 2021; Zhou, et al., 2020). Among engineering materials, polymer composites possess comparatively high tensile strength and elastic modulus (Figure 1.1). These properties become even more exciting when considering the low density, which results in high specific strength.

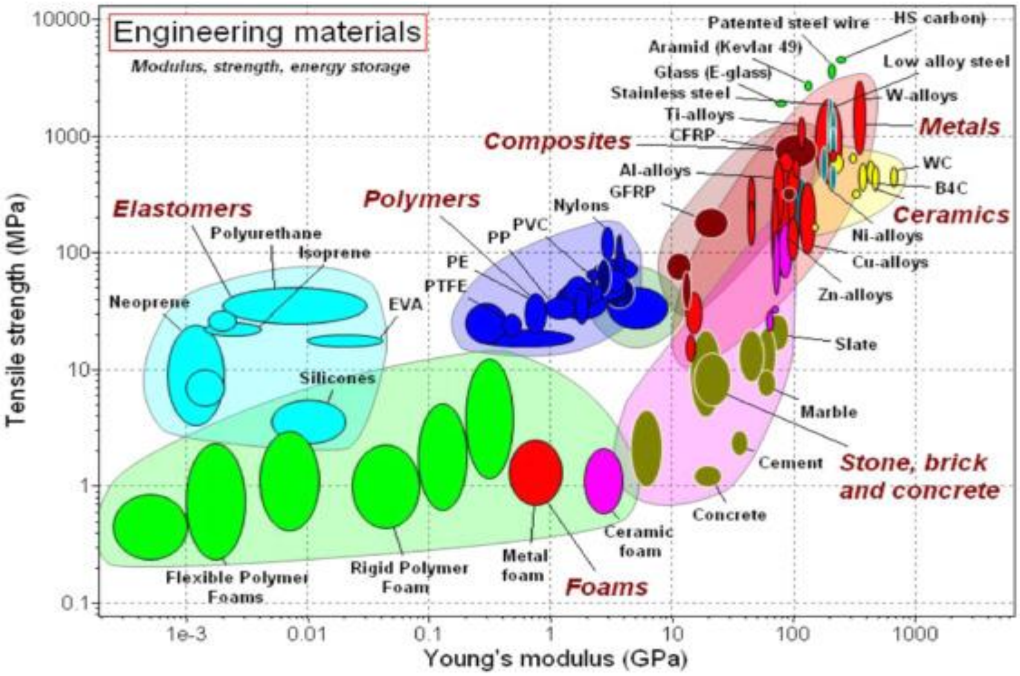

Figure 1.1. Ashby plot of engineering materials highlighting the proficiency of composites, note the position of CFRPs *(Ashby, 2008)*.

Polymer matrix materials have primarily been dominated by thermosets; generally polyester, vinyl ester, polybutadiene, or epoxy resins are used. Epoxy based resins are preferable among high-performance composites, as they offer excellent adhesion to a number of filler types, chemical resistance once cured, good electrical insulation, and do not release volatiles or water during cure (Lubin, 1982). However, in an effort to become more environmentally conscious, thermoplastic polymers are becoming more widely used as they can be reheated and recycled due to lack of cross-linking during processing. Semi-crystalline thermoplastics offer higher fracture toughness, elongation to failure, and shelf life when compared to thermosets (Awais, et al., 2021). Examples of common thermoplastics for composites are polyamide (PA, nylon), polypropylene (PP), polyetherimide (PEI), and polyphenylene sulfide (PPS).

An appropriate manufacturing method for fiber reinforced polymer composites can be selected based on the component size and geometry. The most common process consists of laying of unidirectional ply or prepreg over a tool or mold. Dating back to 1988, automatic tape laying uses robotics to precisely place material over simple mold geometries (Soutis, 2020). This process can also be done by hand, but user error becomes a significant source of defects. Automation lowers cost and drastically decreases the part rejection rate (Chen, et al., 2021). Plies/tape can be placed in alternating orientations, commonly in the 0°, 45°, and 90° directions to increase strength and stiffness, and increase resistance to crack propagation (Hajikazemi, et al., 2020). The assembled component can be placed in a bag of exact dimensions during curing to retain the desired shape. Some processes require the use of an autoclave to cure parts under elevated temperature and pressure, but autoclaves can be expensive and require precise knowledge to use effectively. For instance, Boeing has invested a considerable amount into facilities that have autoclaves upwards of 8 m x 37 m to accommodate an entire composite wing of a commercial airliner (Fischtziur, 2015). In effort to avoid autoclaves, vacuum molding or resin transfer molding (RTM) can be implemented. During these processes, pressure drives the uptake of resin onto fibers and is held while the part cures at ambient or slightly elevated temperatures. A laboratory-scale vacuum assisted RTM (VARTM) setup for small test panels is shown in Figure 1a and a diagram of the process is shown in Figure 1.2b.

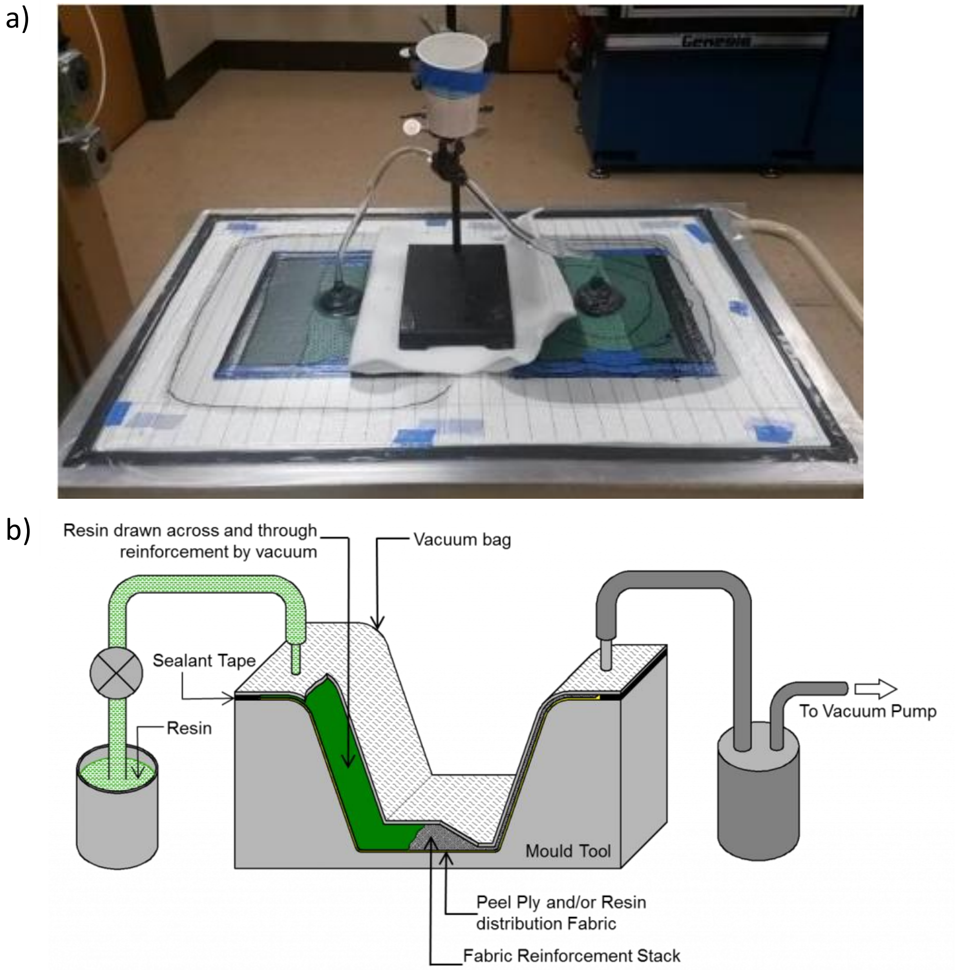

Figure 1.2. a) Small laboratory setup for dual panels using VARTM *(Klosterman, 2018)* and b) a depiction of the process components *(CSIR - National Aerospace Laboratories, 2018)*.

Each of the aforementioned methods of manufacturing have limitations and common defects that are associated with the processing. Parts manufactured via automated tow/fiber placement (AFP or ATP) can undergo path shifting and fiber waviness, creating overlaps and gaps. The overlaps can then become structural weak points. Zhao *et al.* proposes that continuity in fibers is not always optimal and by strategically cutting the plies, fiber waviness can be reduced while retaining strength (Zhao, et al., 2021). Of note, ATP has limitations in curvature during deposition to prevent buckling and distortion of fibers. Designing to contour around holes and other features takes careful consideration. To limit nonconformance in manufacturing, symmetrical laminates are used that are oriented in an optimal performance-related sequence. RTM can result in voids due to insufficient fiber wetting. Moreover, inconsistent thickness at the resin flow front can cause local variations in volume fraction. The introduction of such defects can makes predicting the final component properties challenging. In addition, it can be hard to detect impact damage in composites, as the nondestructive inspection methods may not detect debonds and other defects within the layup (Saenz-Castillo, et al., 2019). To compensate for the unpredictability in component quality as a result of manufacturing, organizations such as the FAA (Federal Aviation Administration) closely regulate testing and repair procedures applied to composites. New manufacturing technologies require rigorous verification, but a method with high reliability and predictability would be a great improvement to the current standards.

1.2 Additive Manufacturing

In the previous section, conventional methods of manufacturing components of polymer composites were discussed. The current section focuses on AM technologies, which is an umbrella term for manufacturing processes in which material is built up one layer-by-layer into a desired geometry (ASTM Standard F2792, 2013). Presently, AM can be considered a viable method for near-net-shape fabrication of components from polymers, metals, and ceramics. Figure 1.3 shows a categorization of AM technologies and the materials they support. There are seven main AM methods, which are categorized in terms of the mode of material deposition and solidification techniques; these processes can also be organized by the raw material state (solid, powder, or liquid systems). Methods such as vat polymerization and powder bed fusion can be further divided into sub-categories as described in Figure 1.3. Although nearly all material systems can be printed, the technology has not yet developed to a point where one method can be used to create components of all material forms.

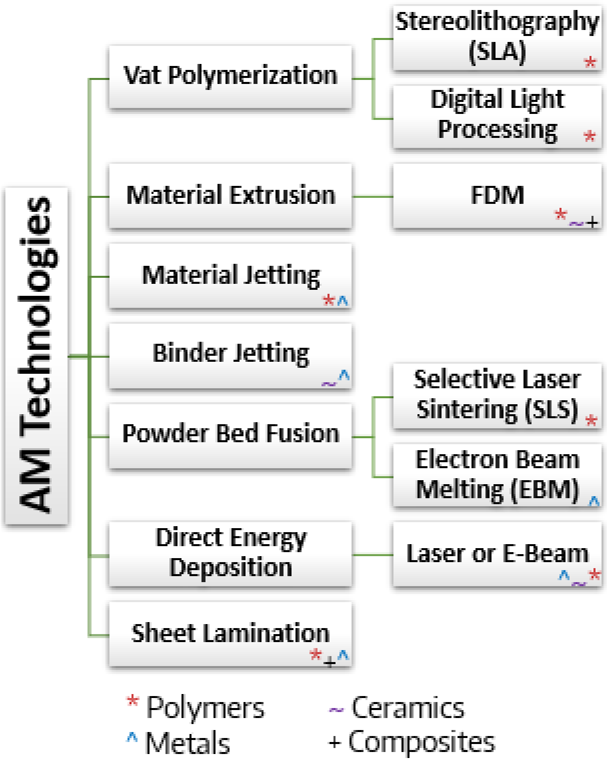

Figure 1.3. Diagram of AM technologies with principal material systems.

Vat polymerization methods use photocurable resins, which can be selectively cured with UV light or laser. Stereolithography (SLA) can have layer resolution down to 10 µm, leading to excellent surface finish (Wang, et al., 2017). However, the process is limited to a select group of resins. Material jetting and/or binder jetting involves spraying resin or binder (deposited onto a powder bed) in the form of droplets, which are cured upon deposition to the build plate. In material jetting, a larger quantity of material is deposited and cured. This method is faster than SLA, although both utilize UV light. Binder jetting adheres granulated forms of material together. Consequently, post-processing is an essential step to consolidate voids and fully solidify parts (Bhuvanesh Kumar & Sathiya, 2021).

Selective Laser Sintering (SLS) and Electron Beam Melting (EBM) are two popular methods for metal and polymer AM that use powder feedstock. In these systems a laser or electron beam are used to heat the powder particles to achieve sintering or melting. Aerospace and automotive industries are just beginning to implement EBM AM. Nevertheless, this is a complex process and the influence of powder reuse on mechanical properties is a topic of importance (Schmidt, et al., 2017; Schur, et al., 2021). Directed energy deposition (DED), which also uses a laser or E-beam, melts the feedstock material immediately before it is deposited. This process is commonly used with aluminum alloys within the aerospace and automotive industry and can be used to repair components by melting new material into an existing crack (Gibson, et al., 2015). Lastly, the sheet lamination process involves stacking and fusing 2D sheets of materials into 3D shapes. Examples of some of the intricate and diverse structures that can be created using AM techniques are illustrated Figure 1.4. Overall, AM facilitates the design and creation of innovative components that were not possible a decade ago and enables the use of exceptional material systems.

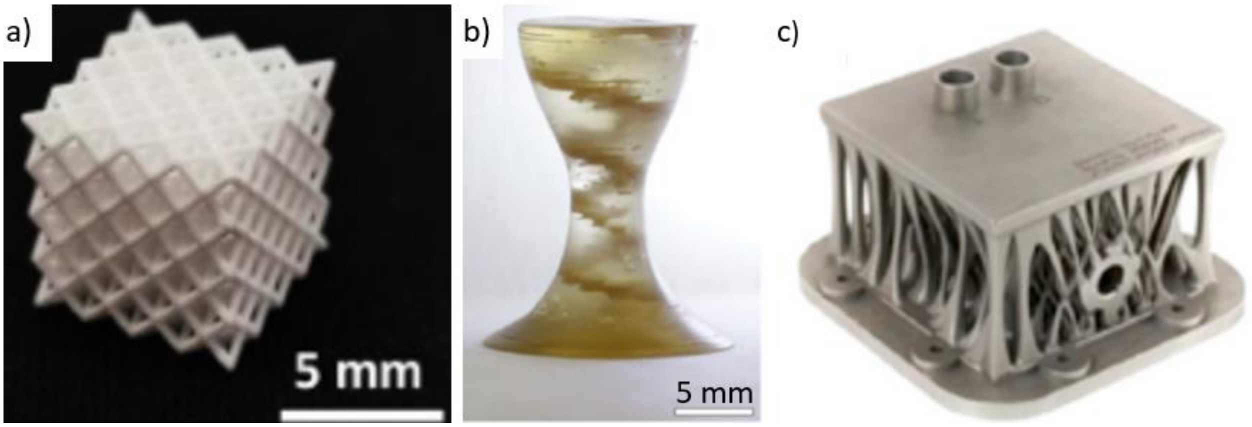

Figure 1.4. Examples of unique structures produced via AM: a) Alumina microlattice fabricated by SLA *(Yap, et al., 2021)*, b) A direct ink deposition of a tailored helical microstructure, additive in polymer is selectively aligned with magnet before cured with light *(Kokkinis, et al., 2015)*, and c) Ti6Al4V part produced via EBM *(Liu & Shin, 2019)*.

Of the various approaches for AM, fused deposition modeling (FDM), i.e., 3D printing, has been widely endorsed for rapid prototyping and modeling. FDM primarily uses thermoplastic filaments as feedstock, which is extruded from a heated nozzle. The molten material is deposited onto a build plate using 3-axes of movement. The FDM process is notorious for producing weak interfaces between layers and inter-track voids between adjacent line depositions, both of which give rise to anisotropic properties (Somireddy & Czekanski, 2020; Tekinalp, et al., 2014; Wickramasinghe, et al., 2020; Ziemian, et al., 2012). These issues can be diminished with appropriate post-process control (Chockalingam, et al., 2016) or accounted for in the design stage (Garzon-Hernandez, et al., 2020). Despite this challenge, FDM is a promising technology, as it offers an opportunity for realizing highly customizable designs in a desktop-size device. Its availability and modularity make it a convenient option for investigating experimental material systems.

1.3 Survey of Composite Additive Manufacturing

In previous sections, polymer composites and methods of manufacturing methods were discussed, as well as the versatility of additive manufacturing. This section addresses the features of composite AM. As a consequence of the potential weight savings and high strength offered by polymer composites, more industries are interested in adopting these material systems. In addition, AM offers design freedom, lowered material waste, and supports the use of an immense library of materials. Notably in search of a lower “buy-to-fly” ratio, the aerospace industry has recently invested in the use of metal AM processes (Dietrich, et al., 2019). Furthermore, since the 1980s aircrafts have increased the use of critical composites structures, especially in wings, tail cones, and fuselage components. Presently, the Airbus’ A350 is comprised of roughly 53% carbon fiber reinforced polymer (CFRP), while Boeings’ Dreamliner is approximately 50% composite (Bachmann, et al., 2017; Marsh, 2007).

In comparison to the rapid advancement of AM processes for metals and polymers, AM processes for composite materials have not yet matured (Parandoush & Lin, 2017). There is tremendous opportunity for AM of polymer composites to be implemented in the production of aircraft structures. If AM techniques could diminish the need for mechanical fasteners by constructing assemblies that are otherwise too difficult, substantial cost and weight savings could be realized (Irving & Soutis, 2020). However, this opportunity requires that AM processes can produce composite components with the desired properties and quality. Undoubtedly, this is a promising area of research.

Considerable research has been conducted on FDM of polymers with discontinuous fibers (Brenken, et al., 2018). . In fact, filaments of polylactic acid (PLA), nylon, and acrylonitrile butadiene styrene (ABS) with short (i.e. discontinuous) fibers are now commercially available. As early as 2001, Zhong *et al.* explored ABS reinforced with glass fibers utilizing a single screw extrusion to create composite pellets, which were then extruded into a filament for use in FDM. They reported that while the glass fibers improved the filament strength, the filament flexibility and handleability were sacrificed (Zhong, et al., 2001). Furthermore, Brenken *et al*. surveyed the field of short fiber reinforced filaments over the past 25 years and provided a summary of the tensile modulus and strength as shown in Figure 1.5a (Brenken, et al., 2018). In general, these studies were limited to common FDM thermoplastics with fiber weight fraction at or below 50%. These filaments are created by blending polymer pellets with fiber reinforcement of desired length and diameter. They are extruded at an elevated temperature that is adequate to achieve the desired viscosity (Ferreira, et al., 2017). Thereafter, the resulting filament can then be cut into small lengths and extruded a second time to increase bulk density (Ning, et al., 2015; Tekinalp, et al., 2014).

The mechanical response of these composites can be further categorized according to the fiber type. As the fiber is stiffer than the surrounding matrix, it is the primary load bearing component. Commercial glass and carbon fibers are the most commonly explored, which is likely due to their availability. However, there has been some work conducted on vapor grown carbon fibers and carbon nanotubes (Shofner, et al., 2003). The addition of fiber reinforcement substantially increases the tensile strength and modulus of thermoplastic polymers used in FDM with respect to the polymer without fibers (Naranjo-Lozada, et al., 2019; Tekinalp, et al., 2014). However, the aforementioned issues related to FDM processing are still present, including voids between adjacent deposited layers and low transverse tensile strength. The control of fiber alignment is critical to the microstructure and mechanical properties (Tekinalp, et al., 2014). Fortunately, the extrusion process can induce a shear force that results in alignment of the short fibers during printing (Raney, et al., 2018; Mahajan & Cormier, 2015).

In reviewing the range in elastic modulus and strength (Figure 1.5a) of composites reported to be achieved by AM, the 50 wt% PPS/CF system that displays a high tensile modulus (roughly 26 GPa) with a tensile strength of almost 95 MPa. That material is of particular interest in the present study as it provides a benchmark of performance with that matrix and fiber combination. With respect to short/discontinuous fibers, continuous fibers are more effective at stress-transfer between the fibers and surrounding matrix. In addition, they provide excellent rigidity and strength along the in-plane axis. A PPS/CF system with continuous fibers could yield superior tensile properties compared to discontinuous fiber composites, provided that it is printable. Continuous fibers add inherent complexity to the AM process, and filaments with continuous fiber reinforcement are not widely available.

Based on a survey of the literature for research on continuous fiber systems used in FDM, there is limited work in this area, as captured in Figure 1.5b. Importantly, the volume fraction of continuous fibers in reported studies is primarily less than 20%, which is more often described by volume fraction rather than weight. The nylon/CF system produced by der Klift *et al.* had 18% CF volume fraction and resulted in the highest strength (465 MPa) of reported materials and with an elastic modulus of 36 GPa (Der Klift, et al., 2016). Although the PLA/CF filament from Li et al. had a higher fiber volume fraction, 34%, it had a lower strength and modulus. Nevertheless, despite the low volume fraction (8-20%), the additions of continuous fibers resulted in substantially greater tensile strength with respect to pure polymer and those reinforced with short fibers. By closely inspecting Figure 1.5b, with increasing the volume fraction there was no clear correlation to increased strength. That could suggest that there is an upper threshold value of fiber volume fraction, and when passed there are difficulties with filament deposition and interfacial cohesion.

However, this could potentially be mediated with physical and chemical modifications to the continuous fiber (Li, et al., 2016).

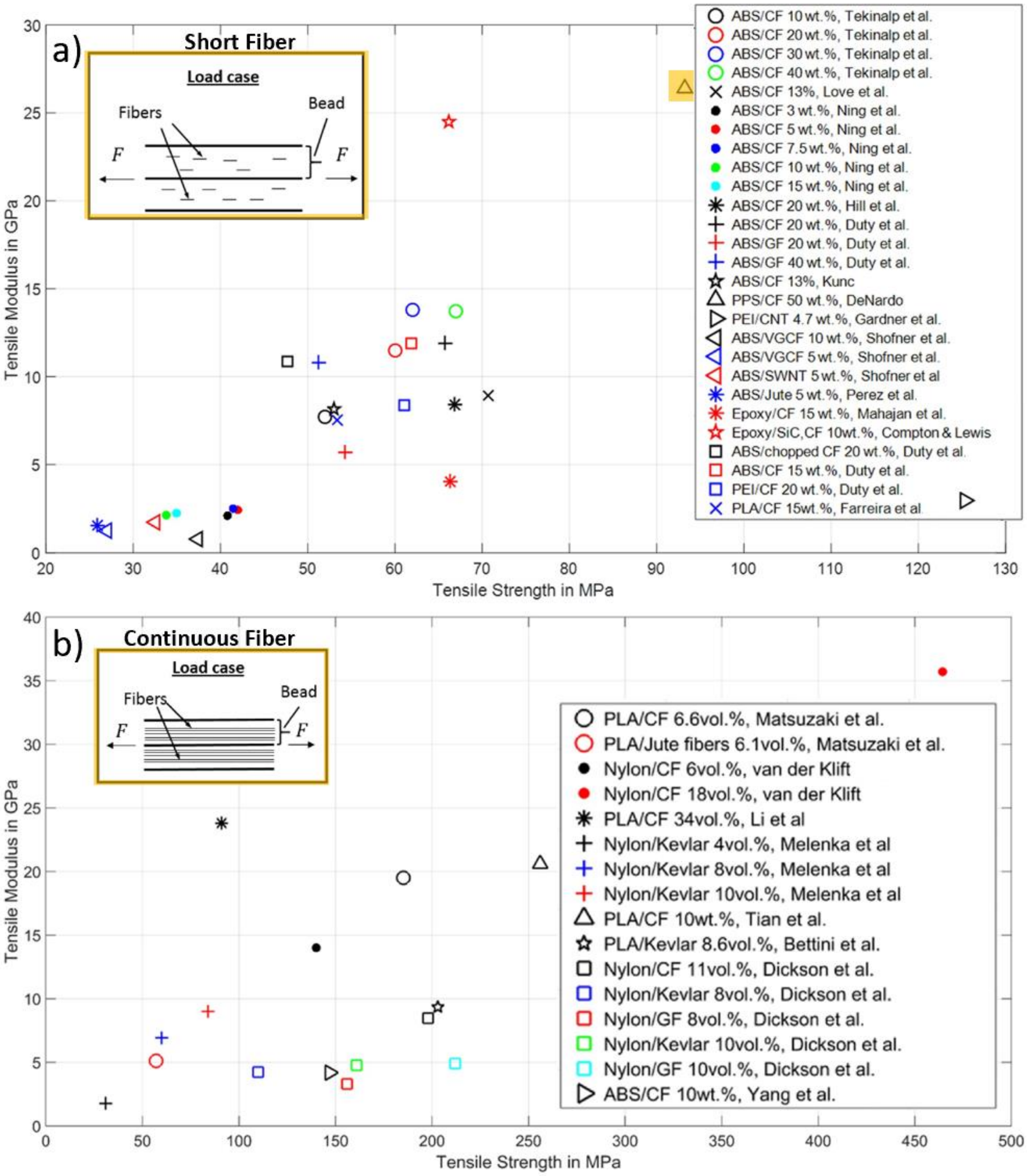

Figure 10.5. Adapted from (Brenken, et al., 2018): Tensile modulus vs. strength in a) short and b) continuous fiber experimental systems.

In general, the existing literature concerning FDM of composites primarily focused on laboratory scale methods of fiber impregnation to produce filaments with continuous fibers. Novel continuous fiber filaments are primarily manufactured within the FDM system (Li, et al., 2016; Matsuzaki, et al., 2016; Hou, et al., 2018; Tian, et al., 2017) An example of a dual extrusion head is shown in Figure 1.6a, where a fiber tow is impregnated directly within the nozzle. For instance, Figure 1.6b displays a PLA tensile bar reinforced with jute fibers, which only marginally increased the modulus and strength over the monolithic PLA. That system is shown as the open red circle in Figure 1.5b. Common defects associated with this method of fiber impregnation and printing include poor fiber wetting and voids between filaments (Matsuzaki, et al., 2016).

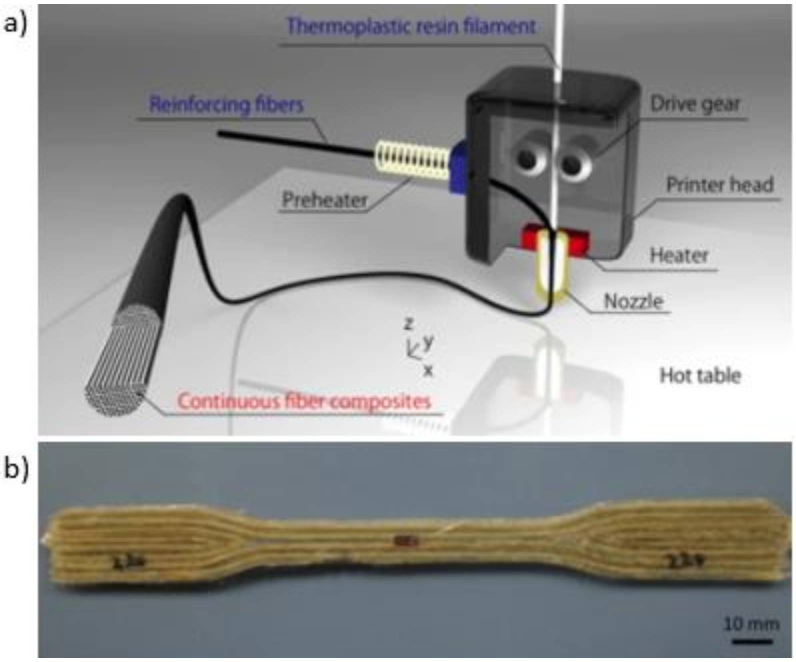

Figure 1.6. Development and printing of continuous fiber composite systems by FDM. a) Model of in-nozzle impregnation of continuous reinforcing fiber and b) a tensile specimen of jute fiber/PLA with a continuous tool path. Taken from (Matsuzaki, et al., 2016).

Similar to the absence of commercially available polymer filaments with continuous fiber reinforcement, there are also few commercial systems that support printing and the production of components with continuous fiber filaments. One is available through Markforged, Inc. (Watertown, MA, USA) with its own proprietary associated feedstock. This system can produce net-shape components with integrated layers of continuous fiber reinforcement (Blok, et al., 2018; Der Klift, et al., 2016), but is currently limited to a 30% fiber volume fraction. In looking beyond conventional FDM systems, companies such as Arevo, Inc (Milpitas, CA) use robotic arms to locally heat and deposit filaments of CF/poly ether ether ketone (PEEK) at 50% volume fraction. In the application of that system a compaction roller follows the deposition head, which reportedly reduces interlayer porosity to less than 2% (Zhang, et al., 2019). Clearly, more research will be required in this area to facilitate the advancement of AM with continuous fiber reinforced polymers.

1.4 Objectives

As highlighted, fiber reinforced polymer composites are a lightweight and high strength material system that has applications in many industries. Additive manufacturing offers the ability to uniquely create complex shapes that are otherwise impossible to achieve and could serve as potent approach for manufacturing structures of composite material systems. While 3D printing of composites with continuous fibers is not yet viable for industrial applications (Wang, et al., 2017), it is hypothesized that the advancement of 3D printing for composites could revolutionize the application of conventional and hybrid composites to the transportation industry, personalized protective equipment for sports, and a myriad of other applications.

In this research, a filament for FDM with high volume fraction continuous carbon fibers was secured from Toray and its printability is explored. The specific objectives are to:

1. Develop the necessary technology for FDM of this new CCF/PPS filament and determine the necessary processing conditions for printing.
2. Evaluate the quality of the printed filament through analysis of microstructure, local and global matrix crystallinity, and printing productivity.
3. Evaluate the mechanical properties of the filament in the unprinted and printed conditions, the variability in strength and contributions to the variability.
4. Identify barriers to achieving an ideal printed filament and explore potential modifications for improving the printing processes.

The first two objectives were conducted in collaboration with Toray and the Tokyo University of Science (TUS: Shinjuku, Tokyo, Japan) in effort to investigate the CCF/PPS filament and work towards product improvement and development. Working with the original material supplier offers a unique opportunity for the investigation to directly influence material production. The second two objectives were conducted in consultation with Toray and the TUS investigators, but were conducted independently.

Overall, the results presented in this thesis underscore several obstacles that must be overcome before this composite filament system becomes widely used. However, the controlled micro- and macrostructures offered through AM could provide new opportunities for mimicry of biological composites and the creation of superior synthetic systems. This thesis presents the experimental methodology, details of the material and 3D printing analysis, and a discussion of those results for the novel CCF/PPS composite filaments. While the work concentrates on a CCF/PPS composite, the results should be considered to be representative of those expected in the printing of other candidate continuous fiber filaments in general. Thus, the present research has tremendous potential to impact several sectors of manufacturing.

Chapter 2 – Material Methods

2.1 Filaments

The primary material system explored in this investigation was a 3D printing filament developed by Toray that consists of a PPS matrix reinforced with continuous carbon fibers. The filament has a nominal diameter of 0.6 mm and consists of a single tow of 6000 fibers, which results in a nominal fiber volume fraction of 50% (denoted as VF50), with a density of 1.29 g/cm^3. Toray has initially utilized TorayCA© T700s high strength CF (tensile strength = 4900 MPa, strain = 2.1%, and modulus = 230 GPa) and Torelina© PPS (A900 tensile strength = 80 MPa, tensile elongation = 13%). Five different batches of CCF/PPS VF50 filament were received from the manufacturer, consisting of approximately 100 grams each, that were prepared on four separate dates: June 2019, July 2019, November 2019, December 2019, and October 2020. The method of production was the same across batches. Several experimental batches of CCF/PPS filaments were also obtained from Toray with volume fractions ranging from roughly 36% to 44%. To produce filaments with lower volume fractions, the diameter of the pulled filament was increased (i.e., the amount of matrix material was increased) to achieve the desired CF volume fraction; thus, the number of fibers was the same. These supplementary batches were used to examine the importance of fiber volume fraction on the printability of this new material system. Furthermore, the PPS matrix utilized in the composite filament was also provided by Toray in the form of raw pellets, along with 1.75 mm and 0.6 mm diameter PPS filament.

The commercial material evaluated in this investigation was a continuous carbon fiber filament marketed by Markforged. This material served as a market standard for CFRTP and is included in this investigation as a control. The Markforged filament consists of nylon reinforced with a 1000 fiber tow, which was experimentally determined. For convenience, it is referred to as

MF. The MF filament has a diameter of approximately 0.4 mm and a density of 1.4 g/cm^3. No details are available on the carbon fibers in this filament. A side-by-side comparison of the microstructures can be seen in Figure 2.1, where VF50 has a significantly more uniform CF distribution.

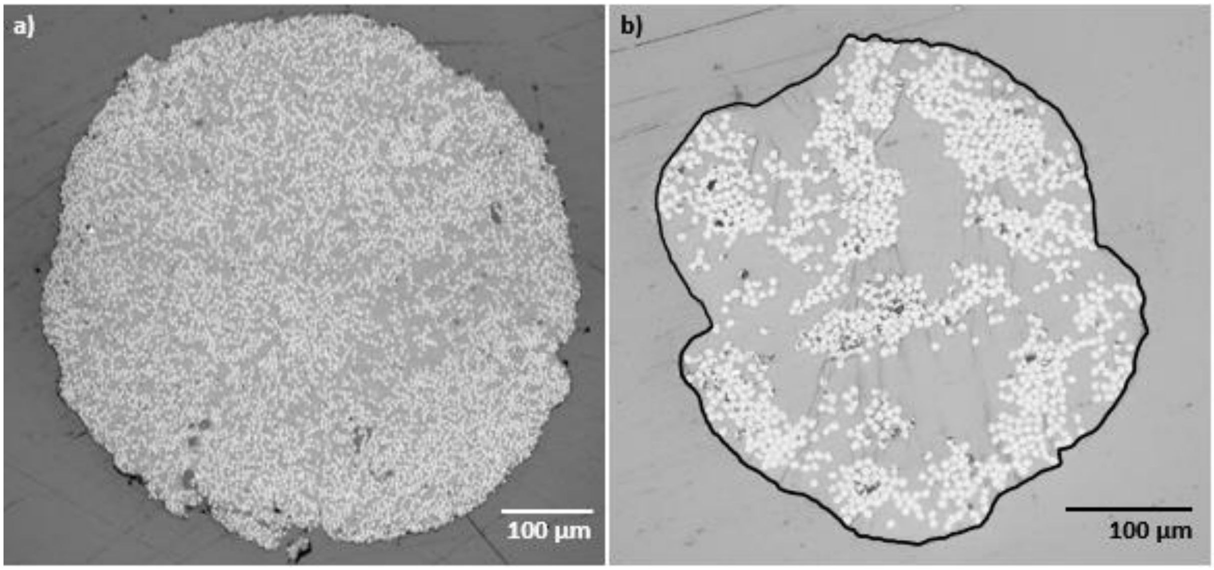

Figure 2.1. Magnified (20x) cross-sections of as-received a) Toray VF50 and b) Markforged CCF/PA. Note the regions of matrix in the center of the MF filament.

2.2 3D Printer

The FDM system utilized throughout this investigation was a self-assembled commercial printer (Prusa, Model I3 MK3S, Prague, Czech Republic). To achieve a nozzle temperature that is adequate for printing PPS, a Type K thermocouple for high temperature printing was inserted into the heater block. It was also attached to a temperature controller (OMRON, E5CB, Kyoto, Japan) which was mounted to the frame of the printer. The heater cartridge, responsible for the nozzle heat source, was rewired from the printer circuit board to the temperature controller. The temperature controller was powered by an external switch power supply transformer (24 V DC, 15 A,) and a cooling fan was installed and wired to the transformer. Once powered on, the cooling fan was immediately activated and stayed on for the duration of printing. The heater cartridge, heater block, nozzle, and an all-metal heat sink (surrounded by PLA housing) make up what can be referred to as the hot end.

The printer was reconfigured from a Direct Drive (extruder sits directly adjacent to hot end) to a Bowden assembly (extruder separated from hot end and connected via tubing). To accomplish this, the extruder motor (basic stepper motor) was disconnected from the hot end, attached to an aluminum extruder feeder drive with a urethane roller, and secured to the top of the printer frame. Polytetrafluoroethylene (PTFE) tubing with an inner diameter of 2 mm was attached to the feeder drive and used to guide the filament. A smaller 1 mm tube fed this portion directly into the nozzle unit. A bare steel bed was preferred to the steel bed coated with PEI that was provided by Prusa. As such, a 0.5 mm thick spring steel bed (FYSETC, Guangdong, China) was mounted to the understructure replacing the original bed. A diagram of the printer setup can be seen in Figure 2.2.

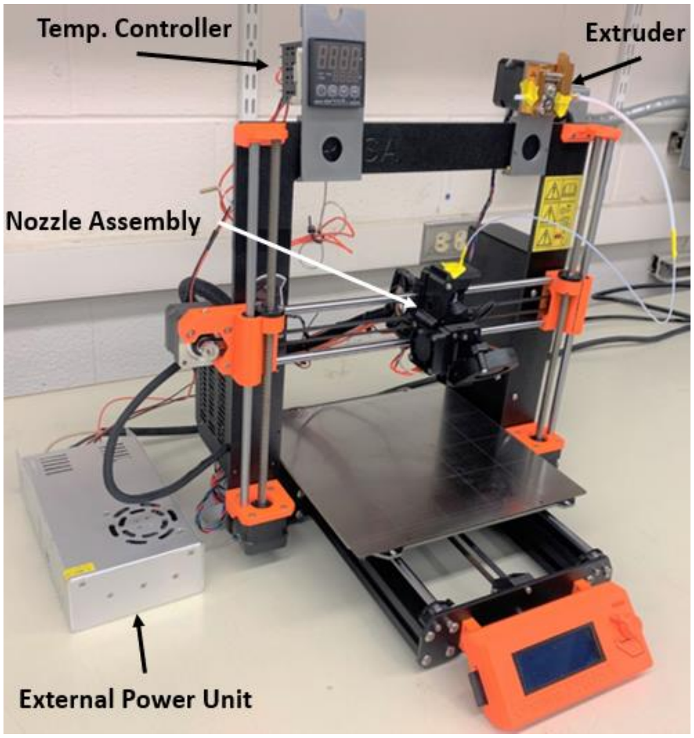

Figure 2.2. Modified Prusa I3 MK3S printer.

2.3 Methods

2.3.1 Initial Analysis

MATLAB (R2020a, The Mathworks, Inc., Natick, MA, USA) was utilized to write basic GCODE commands effective for printing continuous fiber filaments. Basic monolayered structures were coded in this manner, enabling a consistent deposition pathway. Prof. R. Matsuzki of the Tokyo University of Science (TUS) wrote a script for printing 100% dense rectangular specimens at his laboratory at TUS in Japan, which was used for the Prusa printers in the present research.

Prof. Matsuzaki also wrote the basis for an image analysis program to characterize composite filament microstructure, which was manipulated to fit the characterization needs. The program outputs were validated against ImageJ threshold calculations (National Institutes of Health, USA). In the as-received condition, sections from the CCF/PPS and MF filaments were cut into samples approximately 1 cm in length and mounted in epoxy (Epofix HQ Resin and Hardener, Struers, Cleveland, OH, USA) with the sectioned end of the filament exposed. The samples were then polished to a mirror finish using successive etching on a series of fine grit mesh papers (#800 to #4000) followed up by final polishing with a cloth pad and alumina polishing slurry (particle size from 1 to 0.1 µm). An optical microscope (BX51M, Olympus Corporation, Center Valley, PA, USA) equipped with a digital camera (1024 x 768 resolution, Olympus SC30) was used to take images of the cross-section at 20x magnification. A region of interest was set using ImageJ and the acquired images were evaluated using the MATLAB program. Measurements of the CF diameter (already known, validates program accuracy), fiber volume fraction, average fiber spacing distance, and void content were obtained. This analysis was performed with both the MF and CCF/PPS materials, including the filaments with lower volume fractions, as well as samples printed for the various design of experiments that were conducted. The printed filament microstructure was characterized in terms of the CF distribution, which was measured using the MATLAB analysis as a function of distance from the printer platform (bottom surface). The porosity was also evaluated quantitatively from the acquired images and complementary analysis.

A thermogravimetric analysis (TGA) was performed on samples of VF50 and MF filaments using a Q50 device (TA Instruments, New Castle, DE, USA). The TGA was primarily used to determine the temperature at which matrix degradation occurred, but it also provided insight into the thermal behavior of the matrix. Samples between 5-20 mg of as-received filament were subjected to a temperature ramp of 20° C/min to 860° C. Results of the TGA established the maximum allowed temperature for future differential scanning calorimetry (DSC). Once an initial material evaluation was completed, the MF filament was printed using selected parameters. After an understanding of continuous fiber printing was achieved, the VF50 filament was printed.

2.3.2 Design of Experiments

Several Design of Experiments (DOEs) were performed during this investigation to obtain an understanding of Toray's material and its printability. An initial screening study was performed to get acclimated to this filament system and printer, as well as to identify the most important printing parameters that contribute to the overall quality. The screening study was performed according to an 8-run, 6-factor Plackett Burman experimental design and consisted of basic and reflected portions (2x8 = 16 runs total). For each parametric combination, small rectangular monolayer samples were printed, as seen in Figure 2.3. Here, the printed material quality was defined by the surface roughness and presence of interlayer voids. Six factors were chosen, representing key printing parameters, including the nozzle and bed temperature, Z-height (height from the bed to nozzle tip during printing), print speed, material flow rate, and path pitch (centerline distance between adjacent deposited rows). The parameter setting for the high and low values were estimated from previous printing knowledge. The response factors, namely the surface roughness and visible interfacial voids, were visually inspected and rated on a scale of 1-5, where 1 denoted print failure (i.e., the assigned settings were not suitable for printing and the sample could not be printed) and 5 refers to a smooth and well bonded sample with few to no visible voids. The contrast, sum of squares, and estimated effect were calculated based on the ratings, and the four most influential print parameters to print quality were identified from the normalized sums of squares. These parameters were selected as the factors to be used in a complimentary DOE.

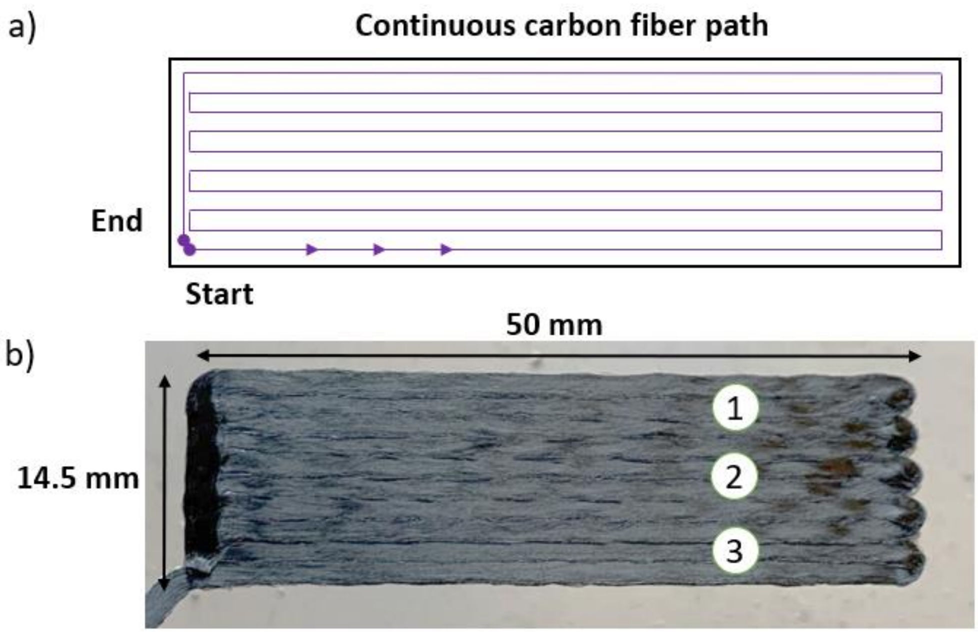

Figure 2.3. a) Schematic of designed continuous tool path and b) a corresponding printed specimen with the positions that were cross-sectioned and imaged during the DOE.

A 3-level 4-factor fully crossed geometric Plackett Burman DOE (Wheeler, 1990) was utilized to characterize the VF50 printability in terms of the printing parameters. This “primary” DOE consisted of low, mid, and high-level 9-run sequences (3x9 = 27 runs total), as summarized in Table 2.1, and was conducted with a batch of Toray material chosen at random from all the batches received. The calculated contrasts and sums of squares for each factor were used to create scree plots, which reflected the relative contribution of each factor to the printed quality.

Two complimentary DOEs, regarded as secondary DOEs, were conducted with the CCF/PPS filaments having nominal fiber volume fractions of 36% and 43%. For convenience, they are regarded as VF30 and VF40 filaments, respectively. The additional DOEs were performed using the low-level 9-run test matrix (1x9 = 9 runs each) and with the exact same values of the printing parameters outlined in Table 2.2. Fully crossed studies were not conducted with VF30 and VF40 due to the limitations in material available. Scree plots were developed with results of these DOEs and used for comparison with those for the VF50 material.

Table 2.1. Factors and their range of values utilized in the primary and secondary DOE.

Factor		Low (-)	Mid (0)	High (+)
A	Nozzle Temperature [°C]	310	330	345
B	Z-Height [mm]	0.20	0.35	0.5
C	Print Speed [mm/min]	150	250	350
D	Flow Rate [%]	50	55	60

Table 2.2. Example of low-level testing scheme, dictating which parameter value to use for each run.

	Contrast			
Run	**A**	**B**	**C**	**D**
1	-	-	-	-
2	-	0	0	0
3	-	+	+	+
4	0	+	-	0
5	0	-	0	+
6	0	0	+	-
7	+	0	-	+
8	+	+	0	-
9	+	-	+	0

The four print factors utilized within the primary and secondary DOE were nozzle temperature, Z-height, print speed, and flow rate. The printed filament quality was defined in terms of the surface roughness, matrix crystallinity percentage, accuracy of printed sample thickness from computer model, and uniformity of the CF distribution across the filament thickness. After printing, sample dimensions were measured using a digital caliper, and the surface roughness was computed using digital microscopy. A small portion of each sample was utilized for DSC to determine the PPS crystallinity. In addition, the printed filaments from all runs were cross-sectioned and run through the MATLAB program to quantify the fiber placement distribution.

The surface topography of the printed samples from the primary and secondary DOE was characterized using a Keyence digital microscope (VR series, Keyence Corporation of America, Itasca, IL, USA). The average surface roughness (S_a) was estimated from the topography over the evaluation area, which is defined according to:

$$S_a = \frac{1}{A}\iint_A |Z(x,y)|dxdy \tag{1}$$

where |Z| represents the absolute value of the profile height from the surface mean (Keyence Corporation, 2020). An evaluation area of 42 mm^2 was used. For each sample, three images were captured along three different locations of the length of the middle row at 4.5x magnification. Each image led to independent measurements of S_a, and these values were averaged to obtain the overall sample S_a of the printed filament at that condition.

The crystallinity of both the nylon (MF) and PPS (Toray) matrices was evaluated using a DSC system (Q20, TA Instruments, New Castle, DE, USA). As PPS is a semi-crystalline polymer, DSC had was of greater importance. Samples of as-received filament, weighing 5.0 mg ± 0.2 mg, were placed in T Zero aluminum pans and loaded into the device. Samples of as-received filament, weighing 5.0 mg ± 0.2 mg, were placed in T Zero aluminum pans and loaded into the device. Samples from the DOE were also prepared in a similar manner. Pure PPS pellets were also subjected to DSC, both as-received and succeeding short thermal treatments (in effort to increase crystallinity). A heating ramp of 20° C/min was applied from room temperature to 360° C and cooled immediately to 60° C at the same ramp. The percent crystallinity was defined from the heat flow versus temperature response according to (Lee, et al., 1995):

$$x_c = \frac{\Delta H_m + \Delta H_c}{\Delta H_m^{\circ}(1 - W_f)} * 100 \quad (2)$$

where,

$$W_f = \frac{m_{cf}}{m_{total}} \quad (3)$$

ΔH_m and ΔH_C represent the heat of fusion (melting enthalpy) and heat of cold crystallization, respectively, and ΔH_m° is the heat of fusion of 100% crystalline PPS, which is defined as 146.2 J/g (Maemura, et al., 1989). Furthermore, m_{cf} and m_{total} represent the sample mass of carbon fibers (back calculated from sample volume and known CF density) and total sample mass, respectively. A Blue M drying oven (ThermoFisher Scientific, Waltham, MA, USA) was utilized in investigating pre- and post-printing annealing of PPS based filaments. The PPS filament can be dried before it is printed, to achieve better surface finish and printability, and is generally held around 100° C for several hours. Following the heat treatments reported by Geng (Geng, et al., 2018), printed samples, as well as virgin pellets, were heated to 200° or 240° C and held for 100 minutes and then placed in the DSC to measure changes in crystallinity.

2.3.3 Mechanical Analysis

Due to the brittle nature of the CCF/PPS, traditional clamping in a wedge-grip apparatus for tensile testing would cause localized failure. In addition, this material system is not yet at a point where a dogbone or other ASTM D3039 (ASTM D3039, 2017) sample can be printed with accuracy. Therefore, a set of tensile grips was designed to enable uniaxial tension experiments on singular filament strands with a universal testing system (Model E1000, Instron Corporation, Norwood, MA, USA) as seen in Figure 2.4. Two iterations of grips were fabricated using a Markforged Mark Two desktop printer (Markforged, Inc., Watertown, MA, USA) and printed using Markforged Onyx material with 55% infill. The grips consisted of mirrored top and bottom mounts with aligned gauge section (~90mm). The grips were rounded to a large enough radius of curvature to avoid filament fracture and also incorporated a flat back panel, parallel to the gauge length, where the filament was clamped. A sample length of roughly 400 mm was needed for testing. The filament sections were sandwiched between portions of aluminum sheet material and sandpaper, which were secured to the grip surfaces of the fixtures using C-clamps.

As this test was experimental, and did not follow a published standard of practice, the grips were validated by testing common PLA filament (displacement rate: 3 mm/min, n = 3). The results were compared to published values. In testing PPS, type 4 tensile bars were 3D printed with 45°/45° 100% infill at 345 °C and tested at a displacement rate of 50 mm/min, according to ASTM D638-14 (ASTM D628-14, 2014). As-received PPS filament was testing in the custom grips at the same rate and compared against the tensile bar. For the continuous fiber filaments, displacement control loading was applied at a rate of 1 mm/min. The load and displacement signals were recorded, and the ultimate tensile strength (UTS) was estimated using the initial filament diameter and load at failure.

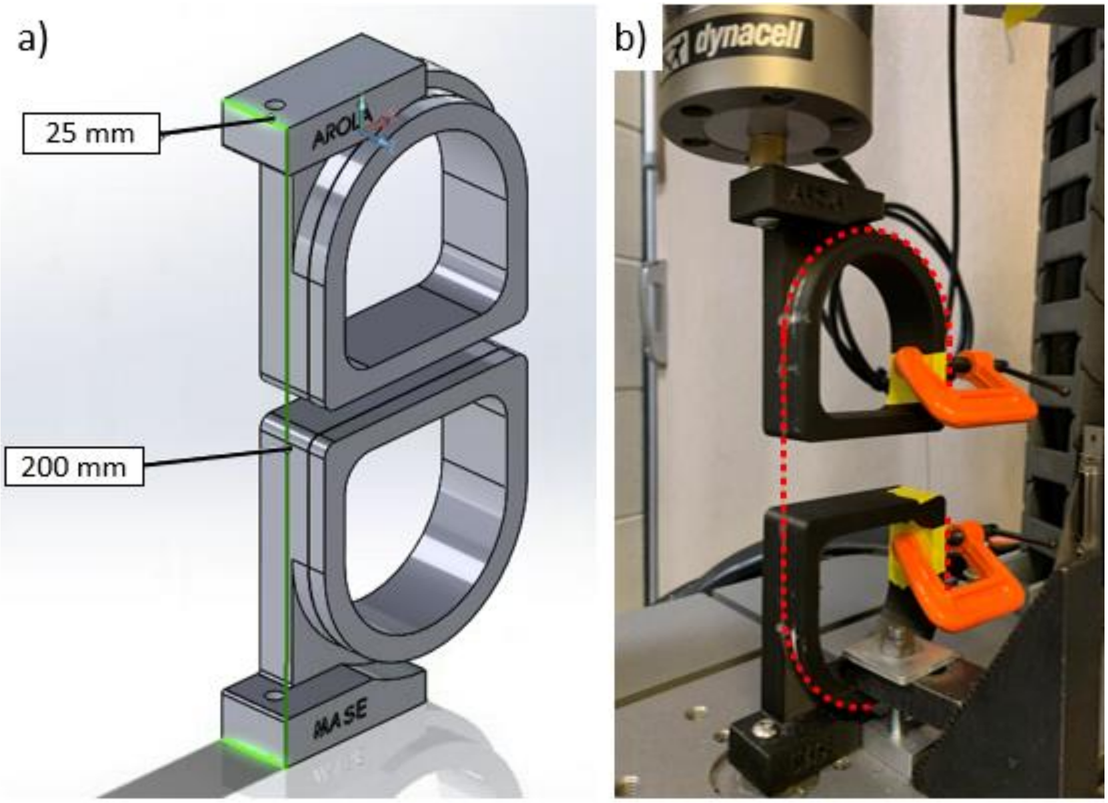

Figure 2.4. a) CAD model and b) physical setup of custom tensile grips for testing uniaxial properties in polymer and composite strands.

During testing, a significant amount of fixture-filament slip occurred as the clamps could not be aggressively tightened without damaging the filament. Hence, digital image correlation (DIC) was adopted and applied on as-received filament to capture a representative accurate strain. To prepare the filament for imaging, precut samples were dipped in white acrylic paint, creating a thin even layer, and quickly dusted with black ink toner powder. The powder had to create a dense field of small particles on the entirety of the filament surface. The samples were left to dry at ambient conditions overnight. An IDS camera (UI318xCP-M, IDS Imaging Development Systems Inc., Obersulm, Germany) and appropriate lens was used for image acquisition. The camera system was set up perpendicular to the filament, within 30 cm of the filament center, and additional lighting was applied to achieve proper illumination. The camera settings used in this effort were as follows: pixel clock- 200, frame rate- 5 fps, exposure/aperture- minimized, image size- 2592 x 2038 px. Once the filament was mounted in the grips, the tensile test was initialized, and digital images were taken every five seconds until failure. The acquired images were analyzed in ImageJ, where the conversion from pixels to physical distance was set using a known calibration grid. Two discrete ink particles that were roughly on the same horizontal plane and approximately 5 mm apart were tracked as the tensile test elapsed. The engineering strain was calculated according to:

$$\varepsilon = \frac{\Delta L}{L_0} \tag{4}$$

where L_0 is the initial particle to particle distance, which also represents the gauge length, and ΔL is the change in length between the two dots. The corresponding engineering stress was calculated from the load and original cross-section area. Then, the elastic modulus was estimated using uniaxial Hooke's Law according to

$$\sigma = E\varepsilon \tag{5}$$

The estimate of modulus obtained from the DIC measurements was considered the "true" elastic modulus. The modulus estimated from the actuator displacement of this test was divided by the true modulus to create a correction factor. This correction factor was then used to adjust all relevant strain data and the corresponding modulus for the subsequent experiments.

A Weibull analysis was performed using the two-parameter model to further analyze the strengths and their consistency. The two parameter Weibull distribution is defined by:

$$P(\sigma) = 1 - e^{-\left({\sigma}/{\sigma_0}\right)m} \tag{6}$$

where P and σ are the probability of failure and stress at failure, and m and σ_0 are the Weibull modulus and scale parameter. The median rank was used to establish the probability function according to

$$Median\ Rank = P = \frac{Stress\ Rank - 0.3}{Number\ of\ Samples - 0.4} \tag{7}$$

and where,

$$P_f = \ln\left(\ln\left(\frac{1}{1-P}\right)\right) \tag{8}$$

The Weibull modulus and character strength were calculated by plotting P_f, derived from Equations 7 and 8, in terms of the ln (UTS). Tensile tests were conducted on samples from the MF, VF30, VF40, VF50 materials. At least one representative batch was chosen from each month of the provided material, PPS, and an onyx system consisting of nylon with short carbon fiber (Sainsmart, Vastmind LLC, Wilmington, DE). Additionally, the Rule of Mixture (ROM) was applied to investigate differences in the expected tensile strength and elastic modulus of VF50 according to:

$$\sigma_{UTS,ROM} = \sigma_f V_f + \sigma_m V_m \tag{9}$$

$$E_{ROM} = E_f V_f + E_m V_m \tag{10}$$

where V is the volume fraction of the subscripts f and m (fiber and matrix, respectively). The values of the stress and modulus for the pure fiber and matrix were supplied by the manufacturer. Unless otherwise noted, the sample size for each group was 15. Images of the broken filaments were also taken during each round of testing in an effort to categorize the failure mechanisms and material consistency.

The strength of the filaments was characterized in the as-received (i.e. unprinted) or printed state. The Prusa printers could only print sample lengths of approximately 300 mm whereas strength testing required a length of approximately 400 mm. To print a straight line of the required length, two printers were placed facing each other and operated in tandem, with a 1/8 in thick stainless-steel laying atop both print platforms. Utilizing precise timing within the GCODE, the elongated print bed was pulled and pushed (bed movement in y-direction) by the printers until a sufficient length was deposited. In addition, to evaluating the filament strength using the traditional printing process, some tensile tests were performed on material samples to isolate effects of individual components of the extruder and nozzle. Briefly, portions of filament were fed through the extruder only, through the heater block and nozzle only or through the extruder and nozzle assembly only without depositing the material on the printer bed. For these special tests, the printer was disassembled as needed to create sufficient samples. An illustration of the additional test methods is shown in Figure 2.5.

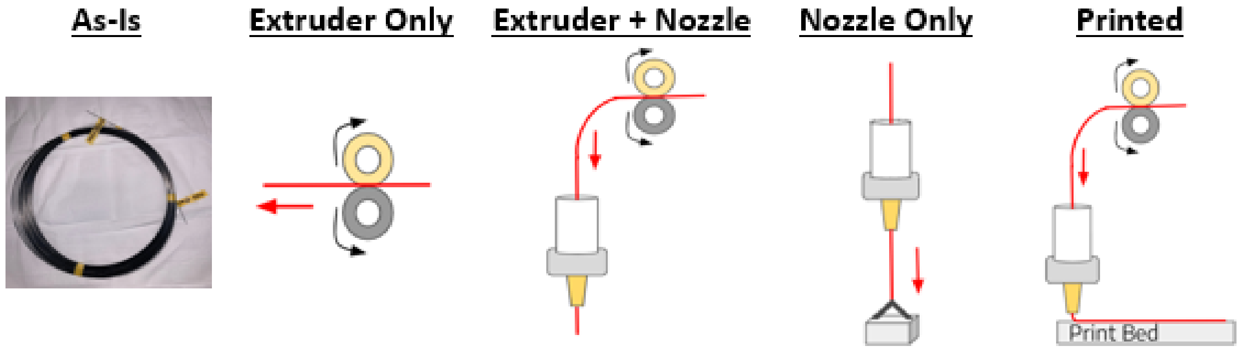

Figure 2.5. Depiction of isolated portions of the printing process that were used to produce specimens and enable characterization of the corresponding effects to the tensile properties.

Chapter 3 – Results

3.1 Material System Analysis

3.1.1 Microstructure

The microstructure of the filaments was evaluated from digital images of the cross-section as shown for a MF filament in Figure 3.1. First, an outline of the filament was performed to establish the region of interest and used to generate a mask. Then, the raw image and mask were imported into the MATLAB program. The MF filament was analyzed first and involved N=10 samples. Through initial troubleshooting and optimization of the program, the fiber content of the filament was determined to be 997 individual CF fibers with an average diameter of 6.24 μm ± 0.16 μm, and with a nearest neighbor distance of 0.70 μm. This yields a fiber volume fraction of 27.04% and with a void content fraction of 0.77%. Based on these results, it is assumed that the MF filament utilizes a 1k tow to create their CCF/PA filament with a VF between 25.5% and 28.8%. As seen in Figure 3.1a, the filament was not perfectly circular and there were generally 3 large matrix-rich areas near the center of the filament, in addition, Figure 3.1b highlights that the porosity is minimal and Figure 3.1c illustrates local variations in fiber VF within the filament. The clustering of carbon fibers is not ideal, and a more dispersed fiber microstructure is desired for more predictable properties.

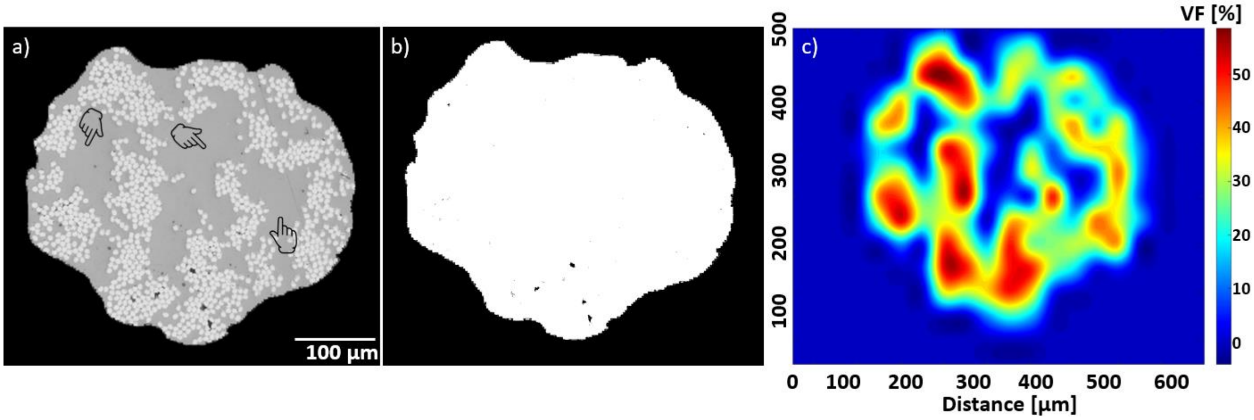

Figure 3.1. Analysis of MF via MATLAB: a) Input as-received filament with matrix-rich regions pointed out, b) mask of filament detecting voids (<1%), c) CF volume fraction heat map, can identify regions of clustered CFs.

The aforementioned approach to filament analysis was conducted on a randomly selected June batch of the VF50 material with n=10. A representative image of the Toray material is shown in Figure 3.2. The results show the provided filament has around 5563 carbon fibers (±173) at a diameter of 4.64 µm ±0.11 µm, leading to a volume fraction of 42%. The found porosity was 0.73% ± 0.56%, and the nearest neighbor distance between fibers is 0.71 µm. There is more variation in this analysis as the carbon fiber size is smaller, with a diameter just within the software's detectable range. Toray later shared that they utilize a 6k CF tow with a CF diameter of 5.1 µm in this filament. With those values, a numerical calculation using a filament diameter of 0.57 mm yields a volume fraction of approximately 48%. While this is not equal to the reported 50% VF, it is still a significantly higher VF than that of the MF filament. Differences in the MATLAB calculated average volume fraction likely stem from carbon fibers that were not detectable (e.g., multiple fibers clustered close together or irregular fibers might have been mistaken for a fiber that was then not counted). Figure 3.2(b) and 3.2(c) also show the porosity and local VF of the VF50, respectively. When comparing to the MF filament, in VF50 the carbon fibers are more uniformly dispersed across the filament cross-section, with fewer and smaller matrix-rich areas (still mostly central). There is some localized increase in VF around the perimeter. The cross-section is not quite circular, when measuring with digital calipers the apparent diameter varied by 0.1 mm. The voids are also smaller than those in the MF filament, although the void content is similar in the two filaments.

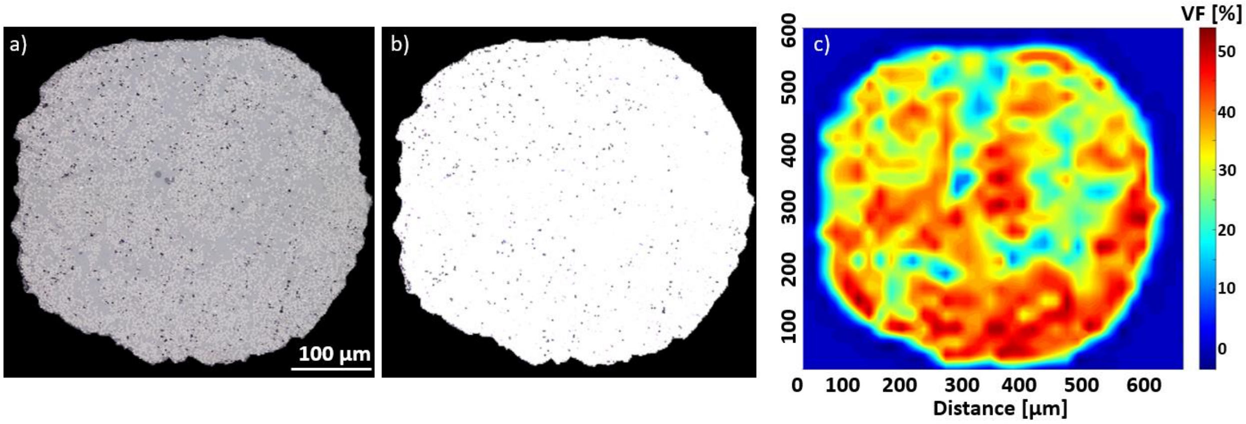

Figure 3.2. Analysis of VF50 via MATLAB: a) Input as-received filament, note an even dispersion of CFs b) mask of filament detecting voids (1.1%), a portion of these speckles were a result of the polishing process c) CF volume fraction heat map.

3.1.2 Thermal Characteristics

Results from TGA on a sample of VF50 revealed an onset temperature at 498.73º and PPS resin was still present upon test conclusion at 860º C. A DSC analysis was also conducted on this filament material, showing a T_m of 283.36º C and T_c of 240.78º C. These values match the thermal properties of PPS provided by the supplier. There was no obvious glass transition and using Eq. 2 the PPS crystallinity was found to be 35.5%. For DSC of the pure PPS pellets, the T_g appears at 90.62 °C. There is a double peak present at melting, which indicates a greater presence of C-O bonds (Brady, 1976; Geng, et al., 2018). Here, the crystallinity is calculated to be 25.69%.

3.2 Design of Experiments Assessing Printability

3.2.1 Screening DOE [CCF/PPS]

The qualitative rating given to the samples for surface quality and side-by-side layer adhesion, along with analysis of 1-way interactions, demonstrated distinct parametric effects on the printability. The basic and reflected scree plots show that nozzle temperature, Z-height, print speed, and flow rate had the most significantly contributions to the print quality. Only flow rate demonstrated significant contribution in results of both the basic and reflected runs, indicating the importance of this particular parameter. Should the flow rate be too fast or too slow in reference to the print speed, a host of defects will be introduced during extrusion and print deposition. While bed temperature and Z-height each have contrast values of opposite signs, this likely indicates 2- and 3-way interactions between parameters which were not included in the DOE for simplicity.

3.2.2 Primary DOE [CCF/PPS]

After identifying the most significant variables from the screening DOE, a more comprehensive analysis was conducted on the VF50 filament. Scree plots describing the parametric effects are summarized in Figure 3.3; the suggested printing settings to maximize the quality of printed filament are listed in Table 3.1. The agreement between the low, mid, and high-level runs indicates that there is a strong correlation between a variable and the factor, which is highlighted using the average estimated effect for each scree plot. This agreement can be seen most clearly in the surface roughness (Figure 3.3a). As evident from the estimated effect, or normalized sum of squares, the Z-height (Z) is most significant to the surface roughness across all levels. The other variables, including nozzle temperature (NT), print speed (PS), and flow rate (FR), are also in agreement, indicating surface roughness is singularly dependent on the Z-height.

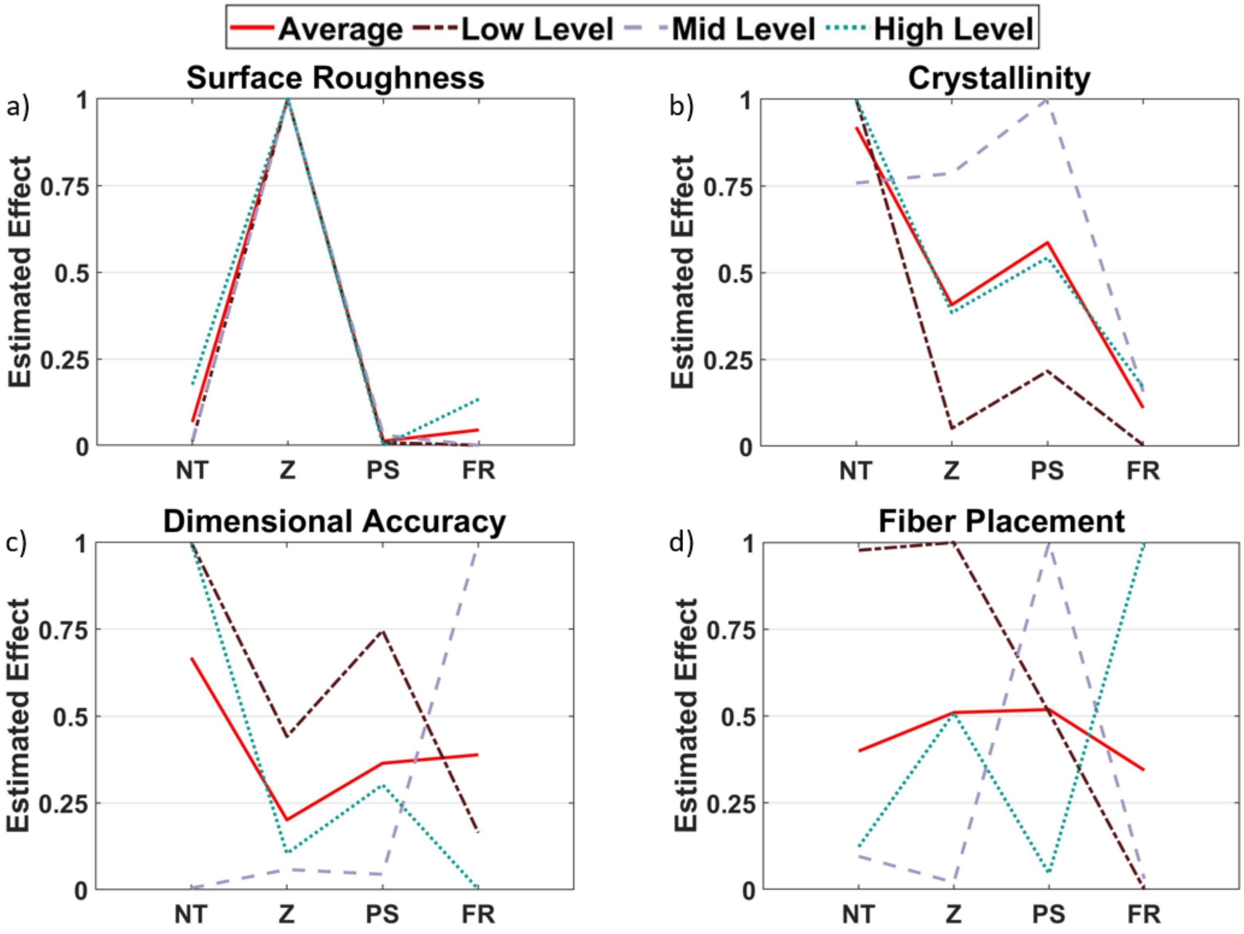

Figure 3.3. Scree plots from the primary DOE for a) surface roughness, b) crystallinity, c) dimensional accuracy, and d) fiber placement. These plots show the normalized sum of squares (estimated effect) for each factor. NT- nozzle temperature, Z- Z-height, PS- print speed, FR- flow rate.

Table 3.1. Summary of DOE factors, suggested settings based on contrast values, and the expected result of setting revision.

Print Parameter	Suggested Settings	Expected Result
Nozzle Temp (NT)	310° C	High crystallinity
Z-Height (Z)	0.2-0.35 mm	Smooth surface
Print Speed (PS)	~200 mm/min	Accurate Thickness
Flow Rate (FR)	60%	Even CF Dispersion

Certainly, the distance between the nozzle and the print bed is crucial to achieving a smooth deposition of the filament. If the nozzle is too close to the bed, the filament becomes compressed to a point that it cannot extrude at the correct rate. Eventually the filament will buckle and break within the nozzle unit, yielding a very poor deposition surface and nozzle clogging. Conversely, if the Z-height is too large, the filament will lack the proper force required to properly adhere to the print bed or previous layer. Thus, the filament will not remain fixed in place on the bed, leading to inconsistencies in the printed geometry.

Optical profilometry shows that the lowest S_a values (10-30 μm) came from a Z-height of 0.2 mm. A closer inspection of the methodology for collecting surface roughness is shown in Figure 3.4. As evident from this image, the printed specimen has peaks and valleys that vary in distance of approximately 1 mm. The heat map generated from the profilometry also illustrates some amount of filament waviness along the deposition path (Figure 3.4b). The waviness has varying degrees of severity depending on the printing parameters. Just by analyzing this one factor, the importance of tightly controlling the printing parameters is demonstrated.

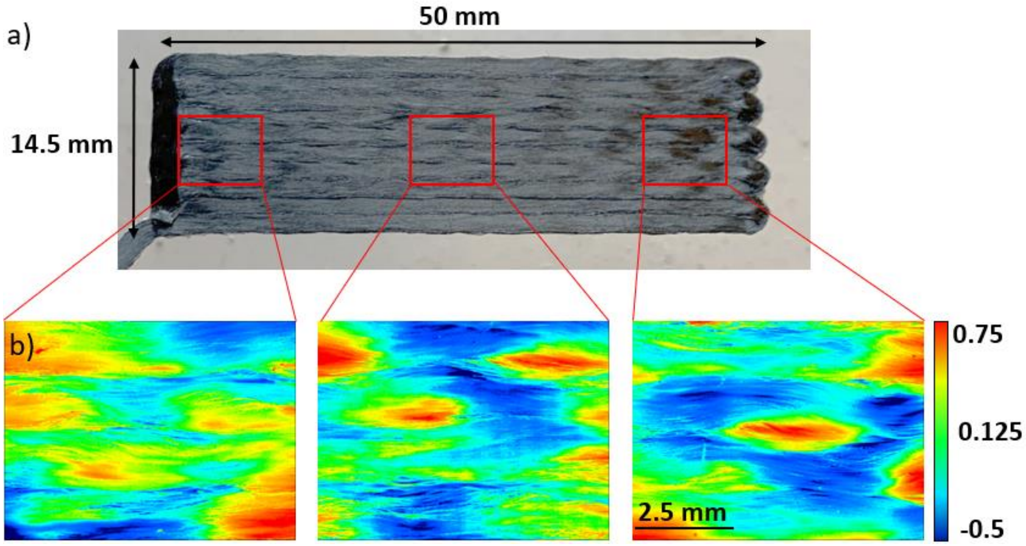

Figure 3.4. The surface topography of the printed composite. a) Image of DOE sample showing set width and length dimensions and the approximate area in which surface analysis was conducted and b) topological results from optical profilometry.

With regards to crystallinity of the PPS matrix, the degree of crystallinity ranges from 15 to 35% when printed between 310º C to 345º C. The same trend in effects can be seen across the three levels of the DOE (Figure 3.3b), i.e. that both nozzle temperature and print speed are the most influential variables. Nozzle temperature appears to be the most significant parameter according to the average trend line. This is not unexpected, as nozzle temperature controls the heat flow into the system and print speed controls the time the filament spends within the heated region. A closer inspection of the DSC thermograph shows that lower nozzle temperatures leads to a decrease in maximum height of the cold crystallization peak (Figure 3.5whereas a higher nozzle temperature shows a larger degree of cold crystallization, suggesting more rapid cooling. This peak is not necessarily desirable as it represents an instability in the crystal state, making the polymer more susceptible to chemical and thermal degradation.

It should be noted that the printer environment is open to the room an exposed to the ambient room temperature and air flow. This can easily affect the sample cooling rate. (Geng, et al., 2018) showed that when printing PPS the nozzle temperature, as well as the cooling conditions, greatly influence crystallinity. As the melting temperature and enthalpy of melting remain largely unaffected by nozzle temperature, the change in cold crystallization is what leads to changes in crystallinity.

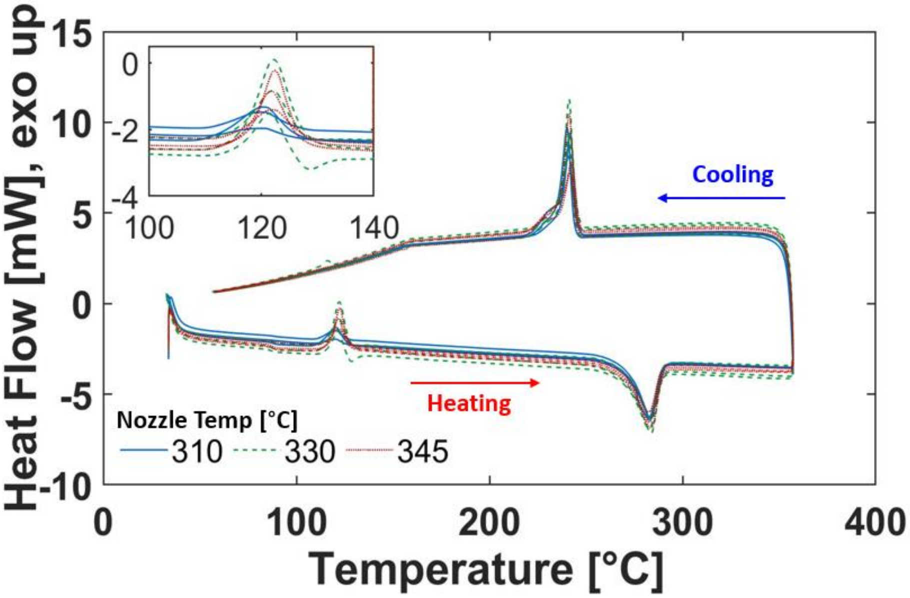

Figure 3.5. DSC curves from low-level primary DOE organized by nozzle temperature, inset of cold crystallization peaks.

The effects of the printing parameters on the dimensional accuracy and fiber placement are shown in Figure 3.3c and Figure 3.3d, respectively. For these two aspects of quality, the effects of the printing parameters appear to be much more interdependent. The factors are too complex to be controlled by a single printing parameter, and the target value of dimensions are only achieved when all variables are at the appropriate levels. In looking at the dimensional accuracy plot (Figure 3.3c) the low- and high-level runs follow a similar trend, whereas the parametric effects at the mid-level are inconsistent. According to the average effects, nozzle temperature, print speed and flow rate are the most significant variables to the printed product dimensions. It should be noted that all of the specimens analyzed met the target dimension within 3% error in the in-plane dimensions (length and width as shown in Figure 3.4a) direction. Certainly, printability (and therefore dimensional accuracy) of this material will in part depend on its apparent viscosity. Viscosity can be a combination of all the printing parameters. Moreover, flow rate and print speed are heavily interconnected as the flow rate must compliment the speed such that the rate of filament extrusion matches the print speed. If this ratio is too high or too low, stresses will build up in the fibers and cause filament waviness or tension leading to breakage. Overall, a lower print speed, with complementing flow rate, allows sufficient time for the filament to adhere to the printer bed, which facilitates accurate placement of the specimen and its dimensions.

The average effects trend for effects of the printing parameters on the fiber placement is almost horizontal (Figure 3.3d). Hence, all four variables have near equal impact on the carbon fiber movement and placement in the final microstructure. Figure 3.6 shows the process in which fiber placement is determined. Similar to the as-received microstructure, the printed specimens were cross-sectioned, polished, and imaged to analyze the final microstructure. The script was then altered to measure individual carbon fiber distances in relation to the bottom surface of the printed filament adjacent to the print bed. Figure 3.6b-c characterize the void content and fiber content, respectively, of the printed microstructure from the digital image (Figure 3.6a). A histogram plot of the fiber frequency as a function of fiber center distance from the bottom of the sample is shown in Figure 3.6d. The fiber placement distribution described by the histogram was then analyzed using a linear regression. The slope of a line of best fit is shown on the plot along with the r^2 value for this particular sample. A slope of zero indicates that an even fiber distribution was achieved across the printed filament thickness and that there is limited fiber agglomeration.

Based on results of the printed filament microstructures of the DOE, the slopes ranged from -7.47 to 0.29 (fiber frequency per vertical height), with r^2 values from 0.02 to 0.7. The mostly negative slopes indicate a trend of more fibers distributed at the bottom of the thickness than at the top of the filament. In order for the fibers to move, the matrix must be sufficiently viscous and a force exerted on the fibers, which happens in the heated zone of the nozzle head upon deposition. When forced through the nozzle tip and placed on the print bed the filament is flattened, getting wider with increasing force and lower viscosity. To better understand the fiber movement, further empirical data and correlation studies are needed. The range of weak to moderate r-squared values illustrates the limitations in using a linear analysis to describe the fiber distribution. A residual plot for each test was also generated to ensure random scatter and that a linear model is adequate. As evident in Figure 3.6e, the fibers follow a normal distribution. Fiber placement in polymer composites can also be described in terms of degree of evenness (intensity of segregation) and clustering (scale of segregation). An ideal system has high evenness and a low amount of clustering (Vincent, et al., 2021). The printed CCF/PPS has good evenness but does demonstrate some clustering. To help facilitate better spacing between fibers the CFs could have a surface treatment that would help with dispersion and matrix-fiber interface adhesion. This of course would add time and cost to production.

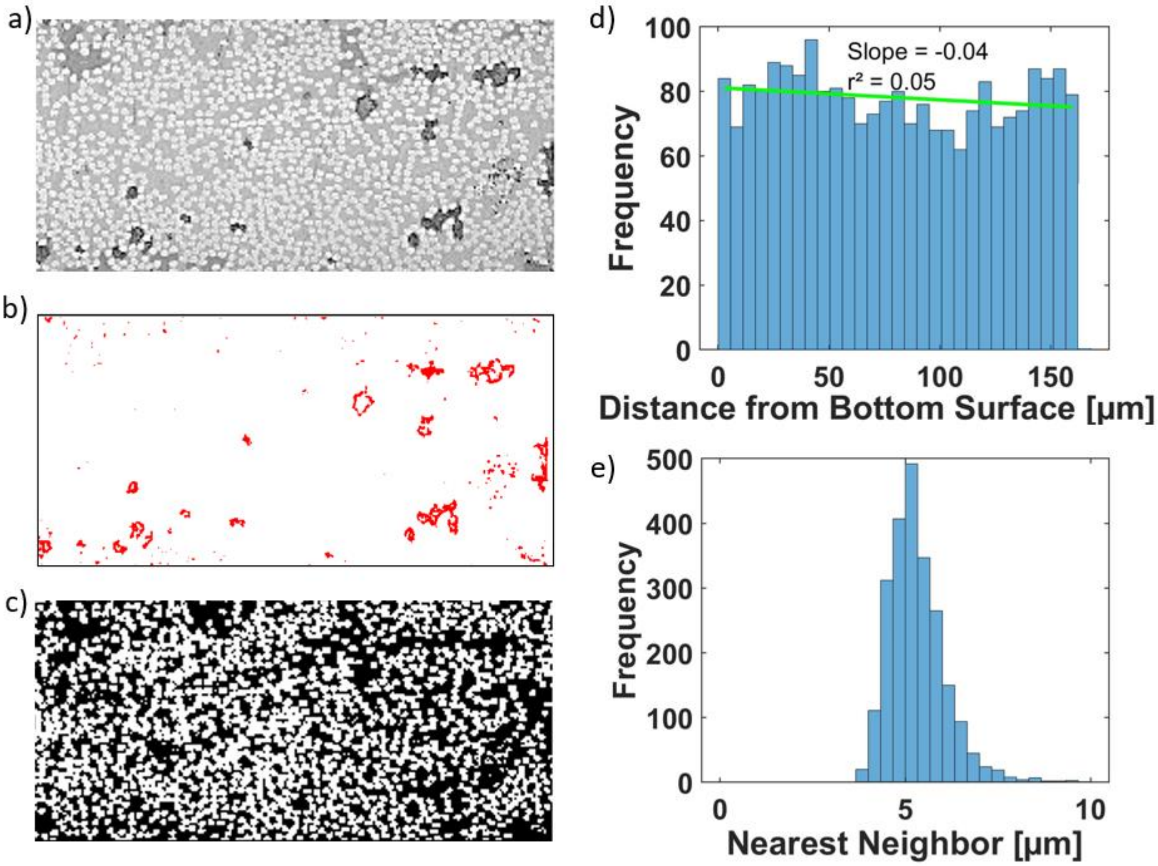

Figure 3.6. MATLAB analysis of printed VF50 filament: a) input region of interest, b) highlights voids, c) identification of CFs from surrounding matrix, d) histogram summarizing CF location in reference to the bottom region of interest e) histogram summarizing CF nearest neighbor.

3.2.3 DOE with Varied Volume Fraction

Once the primary DOE was completed, fractional DOEs consisting of only the low level 9 runs were conducted with the VF36 and VF43 material systems. Results obtained for the estimated parametric effects were then compared with those of the low level of VF50. The results are presented in Figure 3.7 highlighting those for fiber placement, porosity, and crystallinity. Fiber placement and porosity are two critical aspects of the composite quality, and the effects of volume fraction should be understood. Figures 3.7a and 3.7b compare the low-level estimated effects across the three volume fractions. There are some similarities in the scree plots for the three materials, but overall, it appears that parametric effects on fiber placement and porosity are dependent on the volume fraction of the filament. Concentrating on the average effects, nozzle temperature, Z-height, and print speed all contribute towards fiber placement. This is slightly more consistent than the results from the primary DOE, where all four variables contributed to that aspect of quality. While VF36 and VFf50 seem to have similar responses, the VF43 exhibits unique parametric effects on fiber placement. Based on these results, there does not appear to be a trend with respect to fiber volume fraction, unless the VF43 material was an outlier. Similarly, there are differences in parametric contributions to porosity across the volume fractions. The average trend suggests that porosity is largely affected by Z-height and nozzle temperature. Indeed, porosity should be a matrix dominated property in which Z-height and nozzle temperature contribute most to the PPS printability.

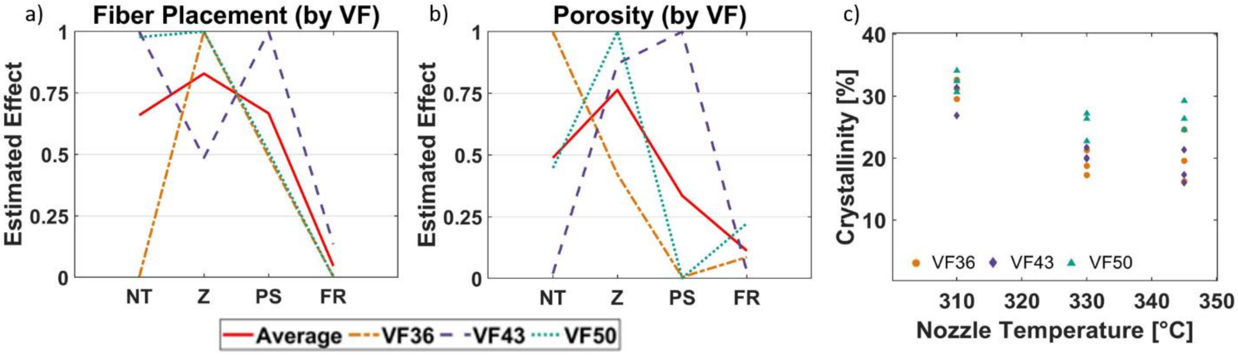

Figure 3.7. Important results from the low-level 9-runs of the secondary DOE for the VF36, VF43 and VF50 materials. a) fiber placement scree plot by volume fraction, b) porosity scree plot by volume fraction, and c) comparison of crystallinity in varying volume fraction as a function of nozzle temperature.

With respect to the other dependent variables, namely surface roughness, crystallinity, and dimensional accuracy, there is a general agreement with the results from the primary DOE. For surface roughness, the Z-height has the most significant effect for the VF36, whereas for VF43 the flow rate is the most significant. For dimensional accuracy, the Z-height and print speed are the most significant for both volume fraction filaments.

Figure 3.7c shows the crystallinity of the PPS matrix in terms of nozzle temperature for all three volume fraction filaments. For crystallinity, the nozzle temperature was notably the most influential parameter for both the VF36 and VF43. According to the distribution, there is a clear trend that the crystallinity increases with volume fraction of fibers. At higher volume fractions there is less polymer matrix present; as carbon fiber is a poor conductor of heat, the PPS becomes the path for heat flow. Thus, when VF50 is passing through the nozzle there is less polymer to dissipate that heat, so it is likely that the PPS is heated to a higher degree than for the PPS in VF36 (more polymer to disperse heat from the nozzle), and the rate of cooling is slower. Conversely, decreasing the volume fraction of CF (increasing PPS weight) results in increasing cold crystallization peaks and therefore decreasing crystallinity. Regardless of the differences in crystallinity, the three different volume fraction filaments had the same degree of printability.

3.3 Mechanical Analysis

3.3.1 Validation of Tensile Apparatus

The 3D printed fixture for tensile testing of the filaments was assessed using a PLA filament with known mechanical properties, as well as Toray PPS filament. The preliminary testing showed that C-clamp grips were required to ensure failure within the large gauge section. The onset of yielding estimated for the PLA with the alternative grip design was 45 MPa, which agrees with the range of reported tensile strength for this material (40 MPa to 53 MPa) (Gunasekaran, et al., 2020). A representative stress-strain curve from tensile testing of the PLA filament is shown in Figure 3.8.

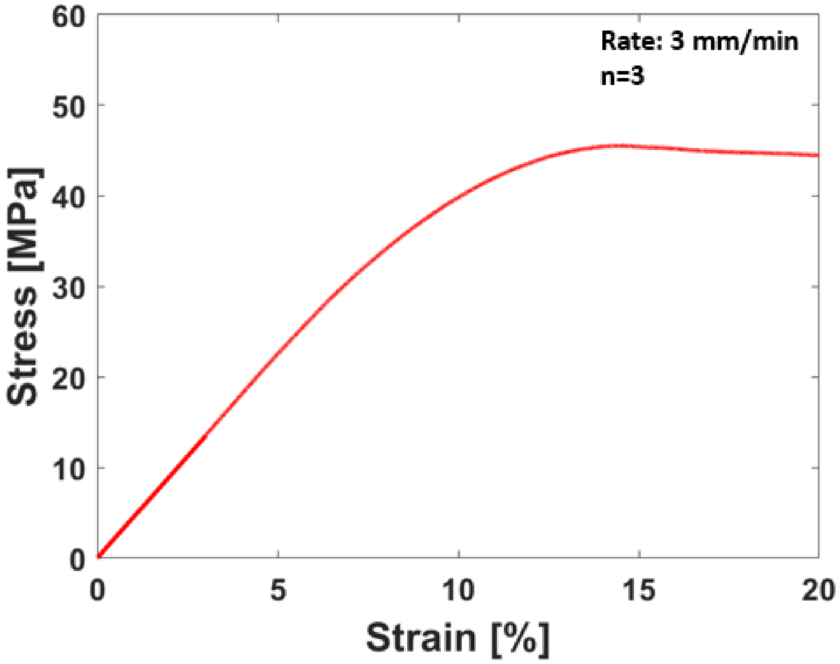

Figure 3.8. Representative strain-strain curve for generic as-received (unprinted) PLA filament.

In addition, the strength of virgin PPS filament (as received from Toray with d=1.75) was compared to that obtained from printed tensile bars that were tested according to ASTM D638. Figure 3.9 displays the stress-strain curve for both forms of specimens, along with images of the failed specimens. The tensile bar specimen, printed at a 45°/-45° infill raster, has an ultimate tensile strength of approximately 61 MPa. There is an initial failure where a portion of the center gauge section fractures, and the remaining portion elongates slightly before ultimate failure. The as-received filament undergoes non-uniform elongation at approximately the same stress (60 MPa) when slight necking occurs, followed by further elongation and failure. In both testing configuration, the elongation involves some slipping of the specimen, more so in the as-received filament. As such, the strain at failure of the filaments involves elongation and slip. Slipping of the specimen in the dedicated grips/clamps occurred throughout the experiments, which is why

DIC was performed to capture the true strain of the composites. Apart from that aspect of the testing, the estimated strengths are very consistent, which provides some confidence in the direct testing of filaments using the newly developed approach.

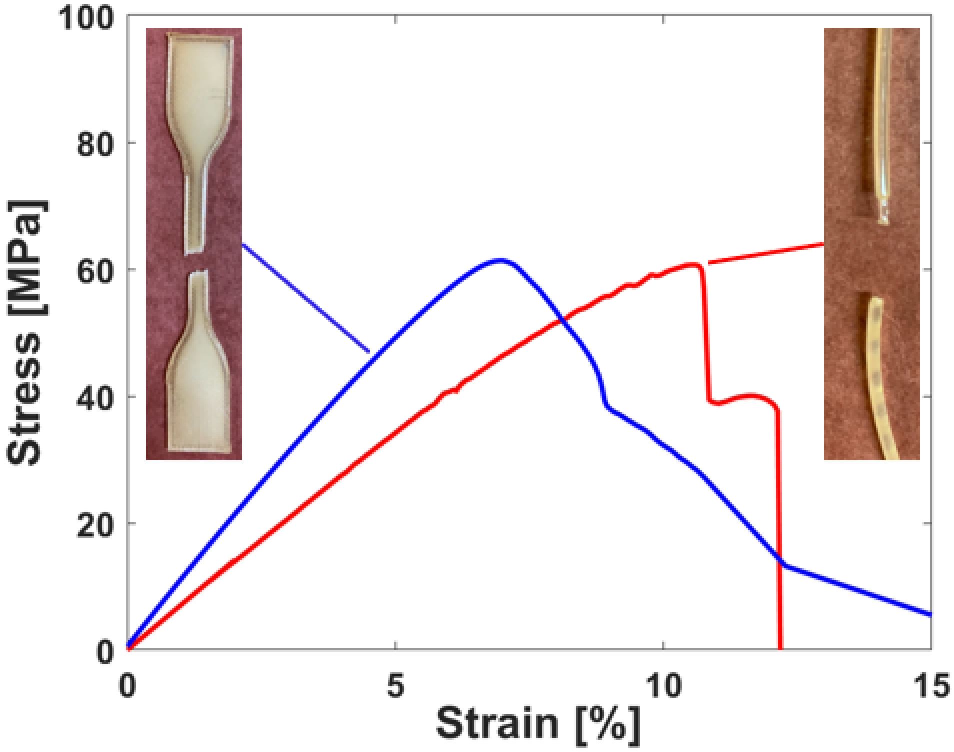

Figure 3.9. Representative strain-strain responses for as-received PPS (red) and 3D printed Type 4 tensile bar (blue) exhibiting similar UTS.

3.3.2 Weibull Analysis

To perform a Weibull analysis and have confidence in the results, an adequate number of samples should be tested. In the absence for an ASTM standard for this type of testing, a sample size of n=15 was chosen. Figure 3.10 displays the stress-strain response for the as-received monthly batches, with the corrected strain from the DIC results and a summary of the results is presented in Table 3.2. The June 2019 batch was the first to be manufactured, and has a smaller strain-at-failure, and slightly higher elastic modulus with respect to the other batches. This particular sample has an elastic modulus of 178 GPa. The remaining batches have a similar mechanical response. Overall, the strain-at-failure ranged from 1.4 to 1.8% and the average elastic modulus was approximately 155 GPa.

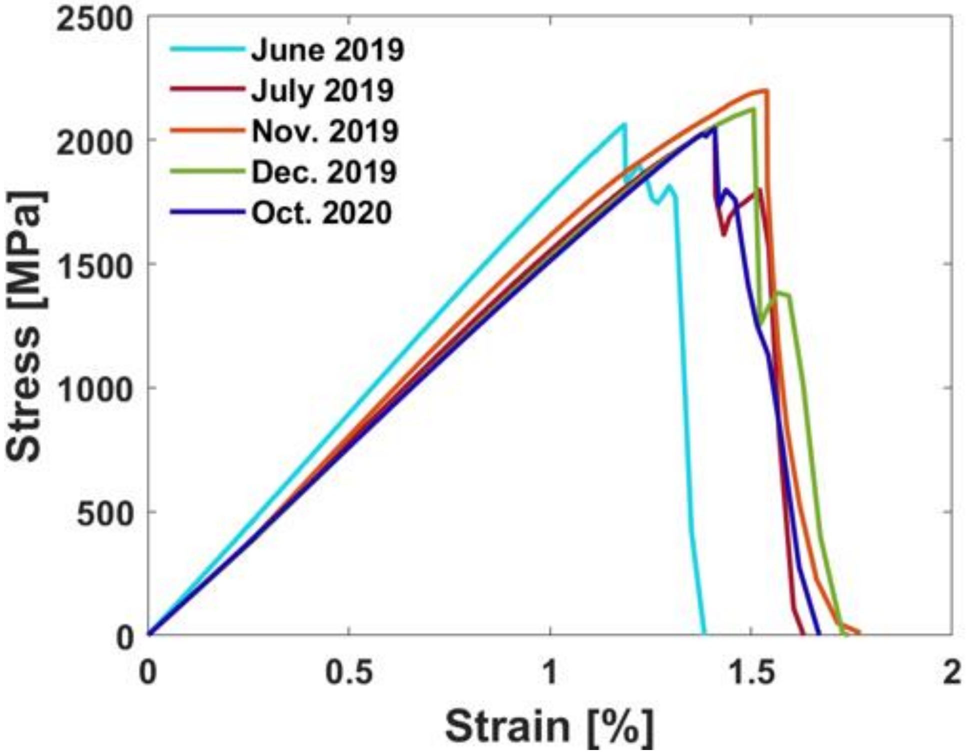

Figure 3.10. Representative stress-strain curves for each VF50 month of manufacture.

Table 3.2. Summary of mechanical results for as-received VF50.

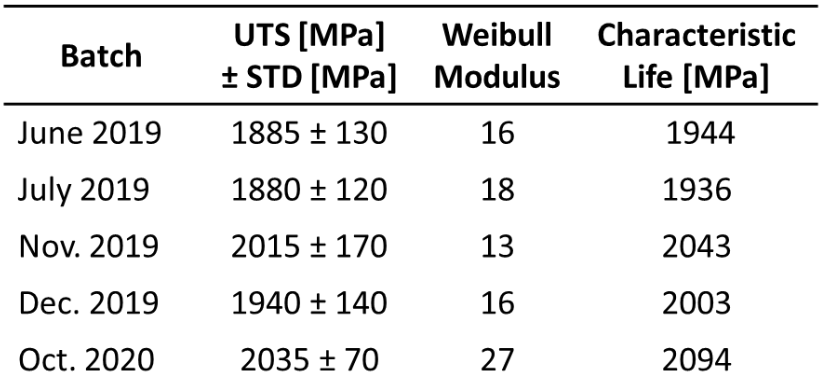

Batch	UTS [MPa] ± STD [MPa]	Weibull Modulus	Characteristic Life [MPa]
June 2019	1885 ± 130	16	1944
July 2019	1880 ± 120	18	1936
Nov. 2019	2015 ± 170	13	2043
Dec. 2019	1940 ± 140	16	2003
Oct. 2020	2035 ± 70	27	2094

The distribution in ultimate tensile strength of the filaments is presented in Figure 3.11a with error bars representing the standard deviation; the Weibull distributions for the batches are shown in Figure 3.11b.

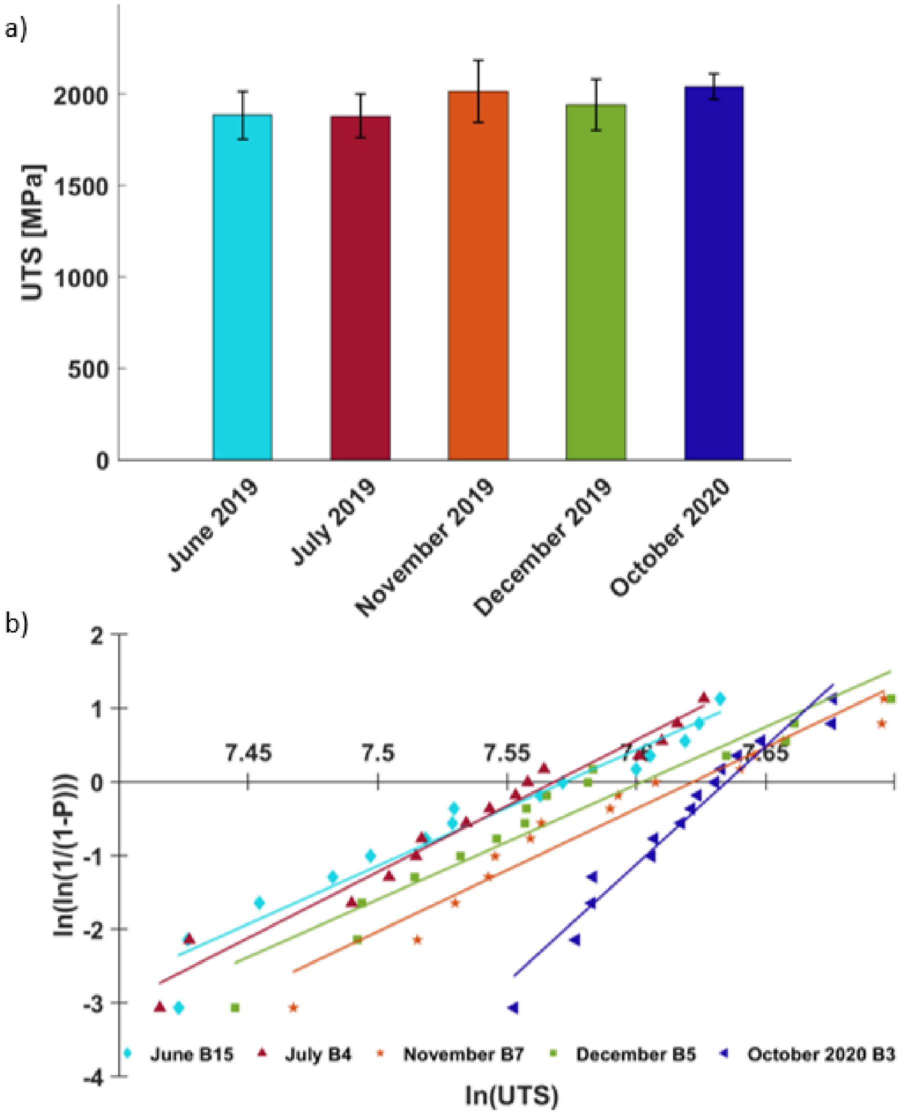

Figure 3.11. a) Comparison of average UTS with standard deviation (n=15) for as-received VF50 and b) Weibull strength distributions for as-received VF50.

Overall, there is agreement between the strength in all the sets of samples tested. The newest manufactured batch has the highest average strength, as well as the lowest standard deviation. Toray has been working towards manufacturing a more uniform and reliable product, and the results of the strength distribution reflect that. All batches manufactured in 2019 have a very similar Weibull modulus, ranging from 13 to 18. This matching slope is an indicator that the family of defects in these batches is consistent. The batch from October 2020 displays a substantially higher Weibull modulus and the largest characteristic life. This high modulus is an indicator that the newest material has more consistent defect family, and less variation in the size or number of defects. The probability curve for the strength distribution is narrower. This is desirable as this material in the virgin state has a more reliable strength. The characteristic life, also known as the value 63.3% of samples will fail prior to, is within a range of 150 MPa (1944 MPa - 2094 MPa).

In addition to the conducting a Weibull analysis on unprinted VF50, a brief ROM calculation was performed to investigate differences between expected tensile strength and modulus to the actual values. Table 3.3 summarizes these differences. While the UTS seen during these experiments is lower than the expected value, the elastic modulus is higher. A decrease apparent tensile strength could be an indicator that there are flaws within the as-received filament as a product of the manufacturing method or the designed tensile apparatus is causing premature failure. Additionally, the significant increase in the apparent elastic modulus could be an effect of the DIC process and the method in which the strain was corrected. On the other hand, the observed overestimation of the modulus could indicate a synergistic effect between the fiber and matrix. Although it is unlikely that this system sees that large of an increase from the ROM value.

Table 3.3. Calculated Rule of Mixture values for VF50 compared to the found values.

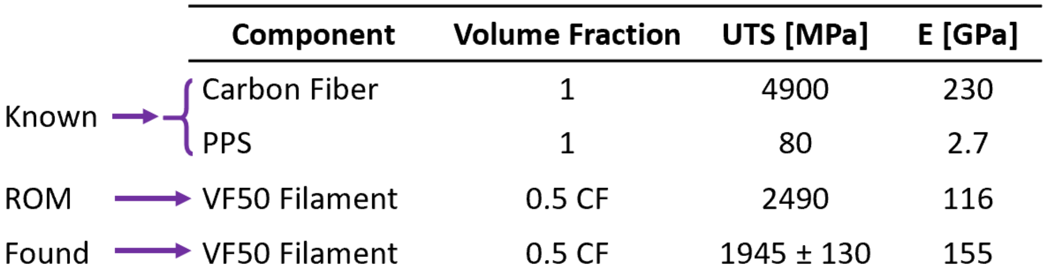

	Component	Volume Fraction	UTS [MPa]	E [GPa]
Known	Carbon Fiber	1	4900	230
	PPS	1	80	2.7
ROM	VF50 Filament	0.5 CF	2490	116
Found	VF50 Filament	0.5 CF	1945 ± 130	155

Another approach used to evaluate the consistency in strength was to evaluate the UTS along the length of the filament. As each sample is approximately 430 mm long, the tensile testing of each batch is conducted over a length of roughly 6 m consecutively along the given spool. Figure 3.12 shows the UTS as a function of increasing test number, or distance along the length for June and November batches. There is no trend evident along the length that indicates changes in UTS along the length. Thus, these batches have an average UTS of 1885 MPa and 2015 MPa, respectively. Consistency along the length could be detrimental as the overall material properties should not change from the start to the end of the manufactured spool.

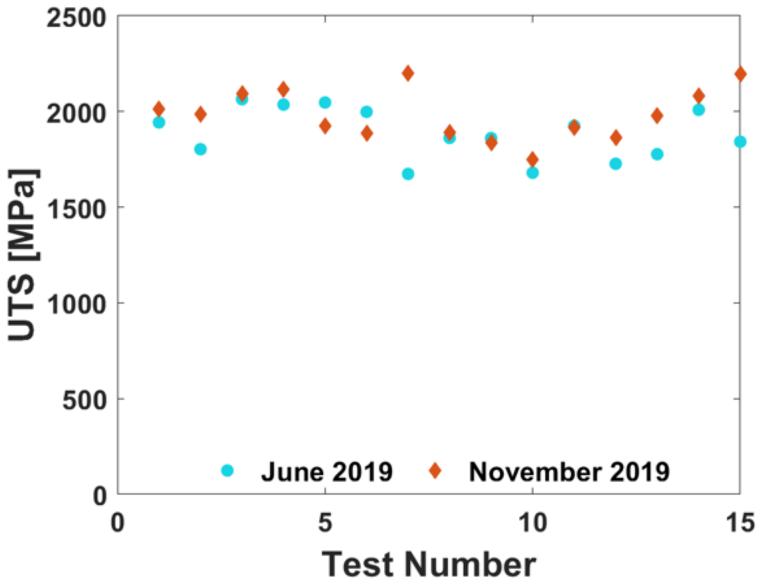

Figure 3.12. The UTS over consecutive tensile tests performed on sections of filament taken sequentially along the length of the batch (n=15 total filament length tested ~6.4 m).

To further investigate contributions to the mechanical behavior, fractography was performed to understand the failure characteristics. Figure 3.13 presents portions of the fractured filaments tested after tensile testing in the as-received condition. The June 2019 batch displays a heavy amount of splaying. The filament fractures in many places and is segmented and into slivers of PPS and carbon fibers. It should be noted that the exact positioning of these pieces is only an approximation and some of the smaller fragments might not have been imaged. The splintering could indicate that there was twisting of the carbon fiber tow during resin transfer. Thus, as the filament was subjected to axial tension, the fibers could undergo interfacial fiber/matrix shear stresses that cause fracture; the matrix could not contain these fibers. The July 2019 batch displays a similar amount of splaying to the June batch. However, the November and December batches exhibited a decreased amount of splaying, and more fractured segments along the length. Although, the filament still split longitudinally in some places, the individual carbon fibers were better contained, which could result from changes in the manufacturing process between the July and November batches. Micrographs of the fracture surface of a sample from the December batch is shown in Figure 3.14. Brittle failure of the fibers is evident from their fracture surface. In addition, there was clear separation between the fiber and the PPS matrix as noted by the green arrow. This suggest poor interfacial strength between the fibers and matrix, which is not desirable but common in some polymer composites (Yu, et al., 2019; Zhao, et al., 2019).

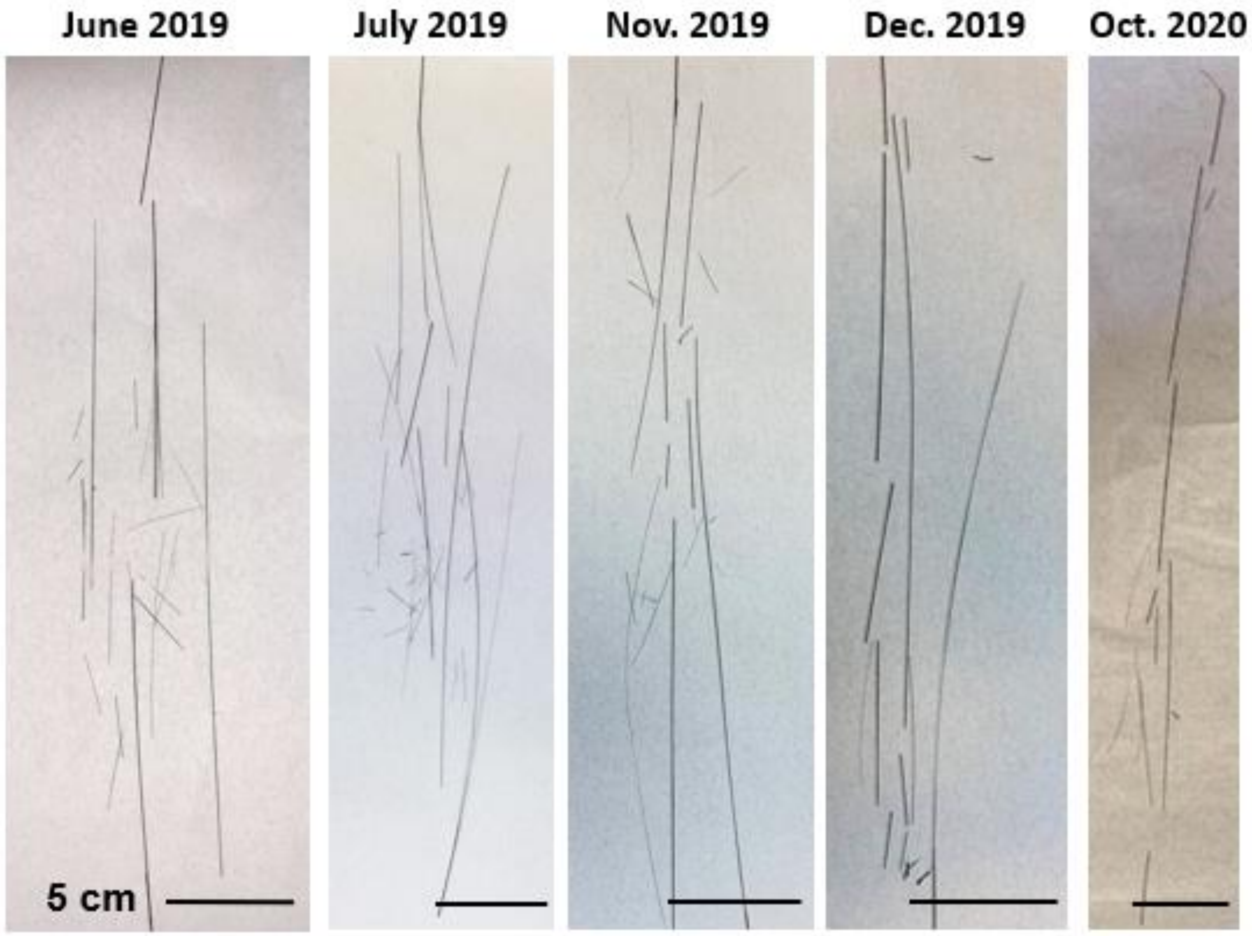

Figure 3.13. Representative fractured samples of VF50 filament tested in the as-received condition.

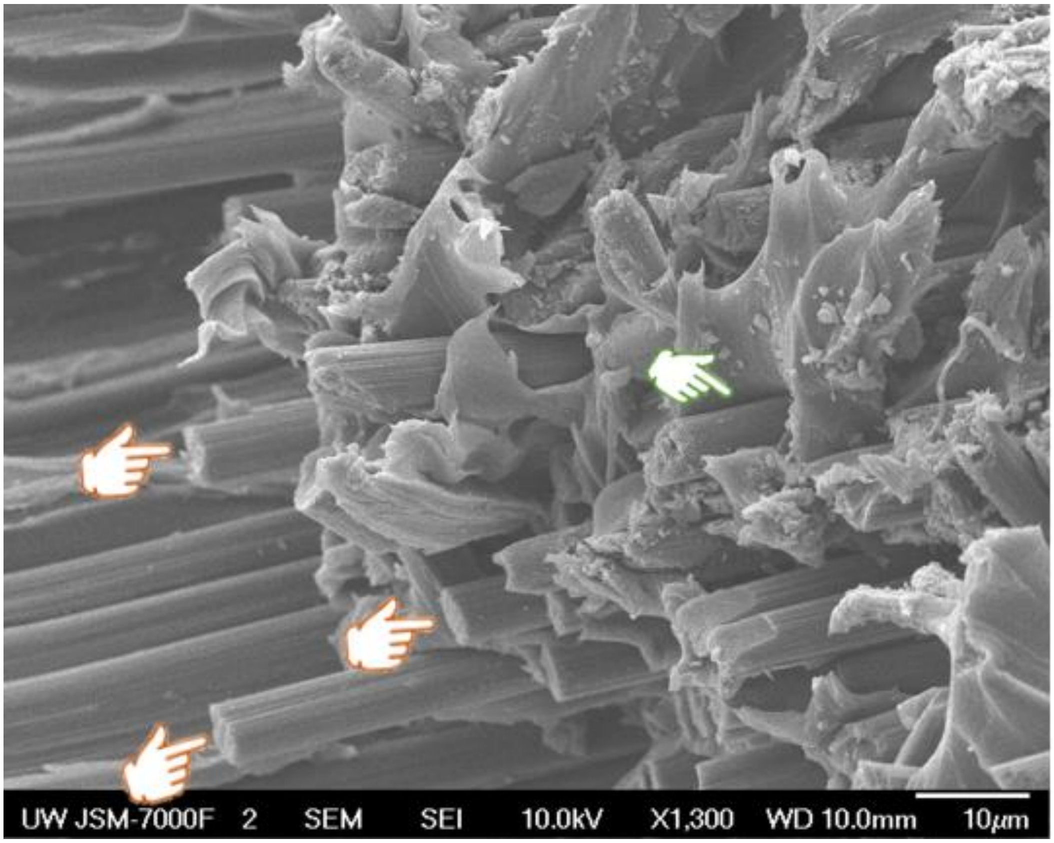

Figure 3.14. SEM of fractured VF50 filament tested in the as-received condition. Orange arrows point towards clean fiber fractures while the green arrow points towards the clean detachment of the PPS from the fiber. In fact, little to no matrix can be seen on the exposed fibers.

In comparing characteristics of fractured filaments across the batches, the October 2020 filaments fractured in fewer places. As evident from Table 3.2, the October batch had higher ultimate strength and Weibull modulus. That suggests that there was a higher degree of consistency in the flaws that served as the root cause of failure, and that there was a consistent number of flaws that contributed to failure in the tested specimens

In addition to the VF50, the supplier provided several batches of filaments with lower volume fraction. Two of these were selected and compared with properties of the June 2019 batch (denoted here as VF50). A comparison of representative \ stress-strain curves for these materials is shown in Figure 3.15a. The VF43 and VF50 samples exhibit a very similar response, with an elastic modulus of 170 GPa and 175 GPa, respectively. The VF36 filament shows a much lower elastic modulus, 115 GPa, and a lower UTS. The strain-at-failure was found to be roughly 1.2% for all three specimens. A comparison of the average UTS for the three volume fractions as well as the Markforged CCF/nylon filament (VF ~28%) is shown in Figure 3.15b. There are two distinct groups of response. The first consists of the MF and VF36, which exhibited UTS of 1415 MPa ± 150 MPa and 1425 MPa ± 120 MPa, respectively. The second group consists of the VF43 and VF50 filaments, which both have a tensile strength that is several hundred megapascals greater, with average value close to 1850 MPa. Interestingly, the VF43 has a higher standard deviation in strength than the other three. With regards to the Weibull modulus of the strength distributions in Fig. 3.15c, the VF43 and VF50 have a similar response. Although the VF36 has a lower characteristic life than the MF filament, it has the highest Weibull modulus. Hence, this material is more likely to fail at a lower tensile stress, but it is the most reliable filament, aside from the as-received October 2020 batch. The MF filament has a low modulus (9) and exhibits a bimodal Weibull distribution, indicating that it has two major families of flaws. The MF filament is much thinner that the Toray filaments, and it incorporates a 1K tow of fibers rather than a 6K tow. In the unprinted state it is more susceptible to damage from handling. Small defects could have been introduced in the specimen preparation process for tensile testing, thereby inducing flaws that were responsible for the different failure modes seen (first four data points of MF data).

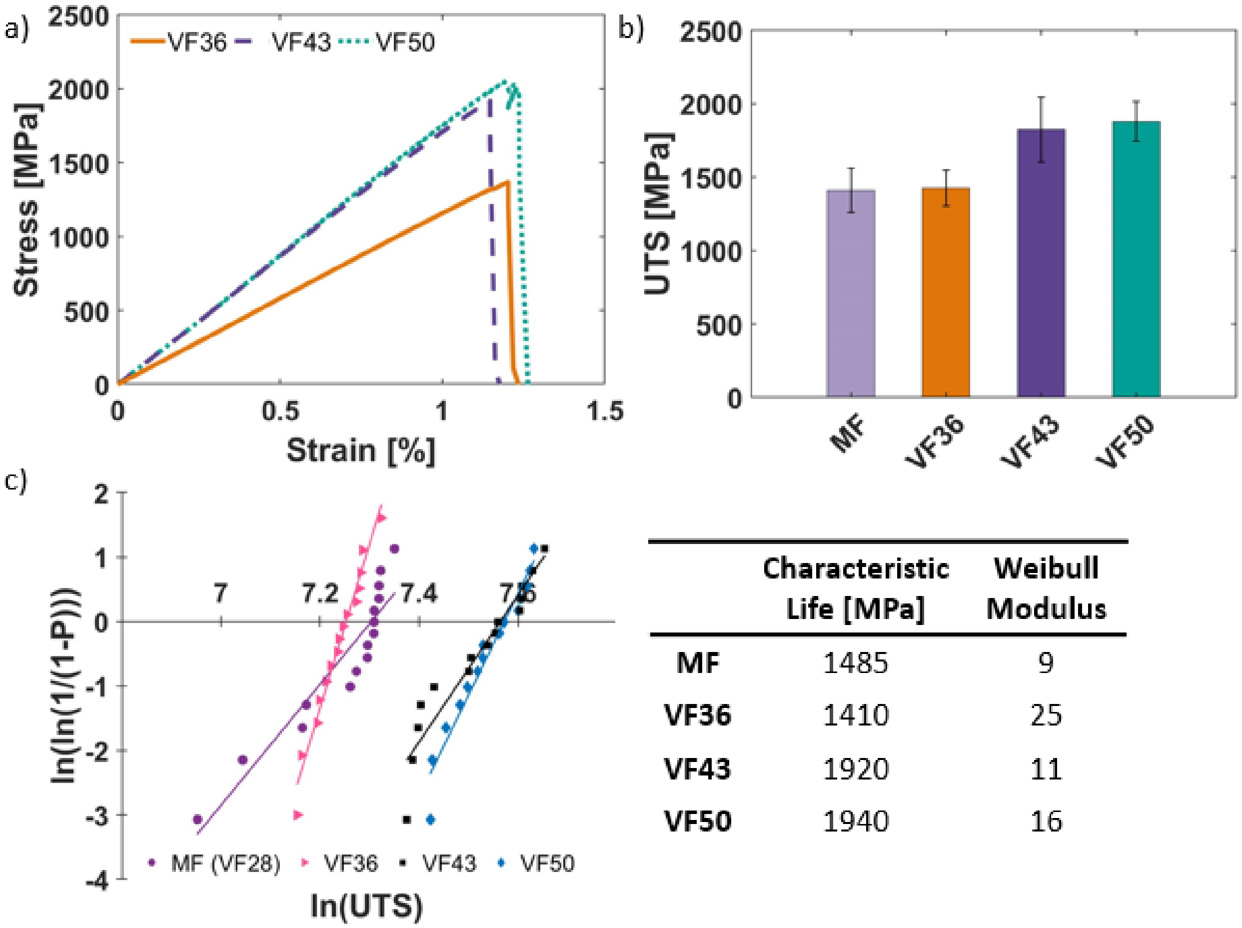

	Characteristic Life [MPa]	Weibull Modulus
MF	1485	9
VF36	1410	25
VF43	1920	11
VF50	1940	16

Figure 3.15. Representative stress-strain curves by volume fraction. b) Average UTS between varied volume fraction and MF with standard deviation. c) Weibull strength distribution with corresponding characteristic life and Weibull modulus.

In comparing the fractured samples of the two lower volume fraction filaments in the as-received condition, a lower degree of splaying was observed. The VF36 fractured into larger discrete sections, as shown in Figure 3.16a. The microstructure for the VF36 filament it is shown in dark field to better highlight the large matrix-rich areas along its circumference. It is possible that the surrounding polymer of the filament shields the carbon fibers from surface damage, which can serve as the origin of failures in testing to fracture. The VF43 (Figure 3.16b) displays a moderate amount of splaying and it has a microstructure more similar to VF50 (Figure 3.16c).

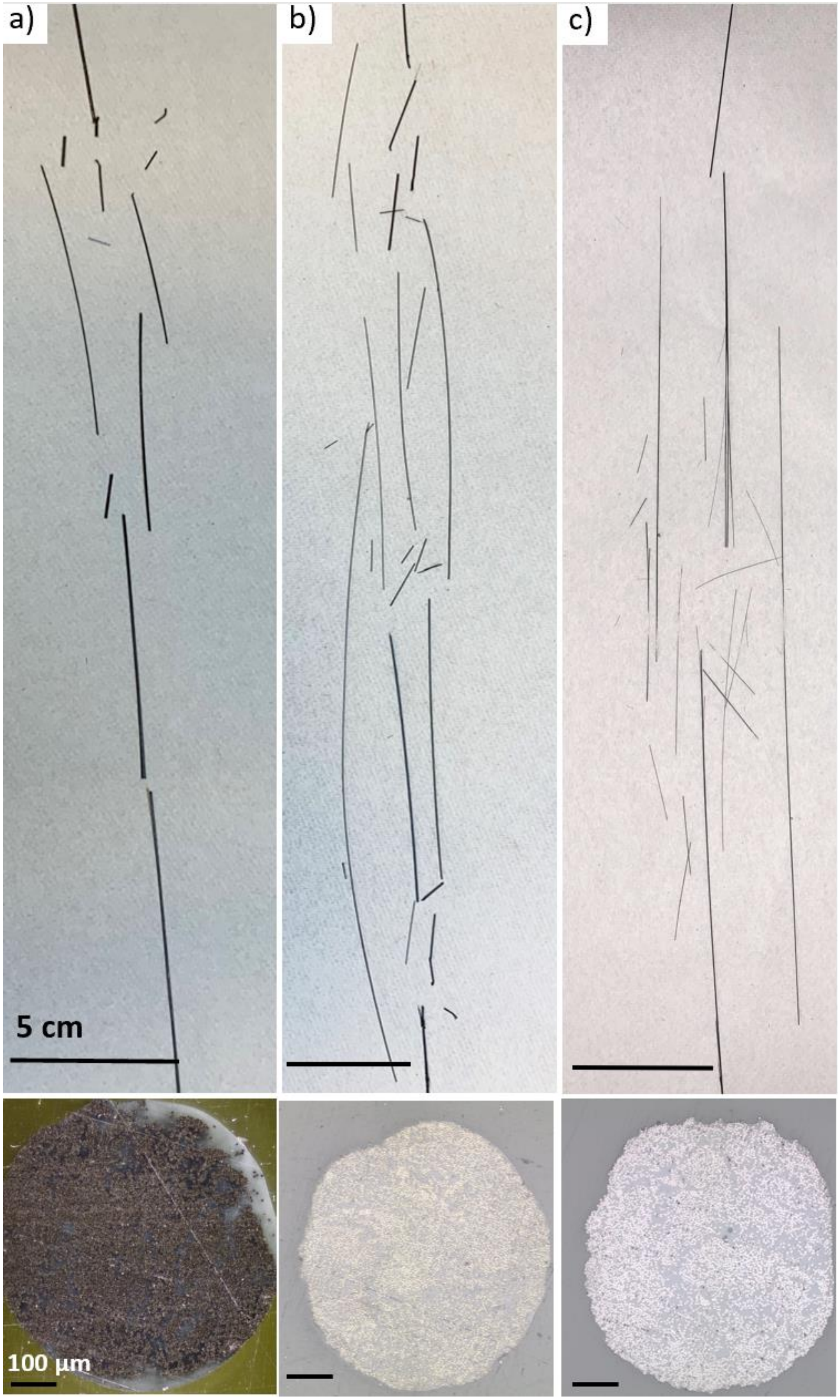

Figure 3.16. Representative fractured filament tested in the as-received condition with the associated batch microstructure: a) VF36, b) VF43, c) VF50.

To compare the effects of the printing process on the tensile response, the tensile strength of select batches of the filaments were tested in the printed condition. Figure 3.17a displays representative stress–strain curves for the printed specimens of the selected batches of material. In general, the failures were very sudden, rather than graceful, with fracture occurring cleanly and into several pieces at an elongation of between 1.1% and 1.2%. The VF43 filament achieved the highest UTS (Figure 3.17b). As previously mentioned, it appears that this filament and the other filaments with lower volume fractions had more matrix material that served to protect the peripheral carbon fibers from damage during extrusion and printing. Nevertheless, there is still a significant decrease in strength that resulted from printing. For the June 2019 batch, a 23.8% reduction in strength occurred; results for the October 2020 batch are similar, with a 20% reduction in the UTS. In comparison, the reduction in strength for the VF43 is only 8.1%. According to the Weibull distributions for strength in Figure 3.17c, the printed June batch has a lower modulus in comparison to the October batch of VF50 and the VF43, both of which have a Weibull modulus near 11. Table 3.3 summarizes the mechanical properties of importance. Upon closer inspection, the Weibull distributions in Fig. 3.17c exhibit bimodal shape. This implies that there are more than a single family of defects that are contributing to the onset of failure. If there are multiple families of defects introduced to the matrix (voids and microcracks) and to the carbon fibers (microcracks, buckling, and twisting), achieving reliability in the mechanical response will be difficult. The feasibility of printing structures with complex geometries and high reliability in performance must be carefully considered.

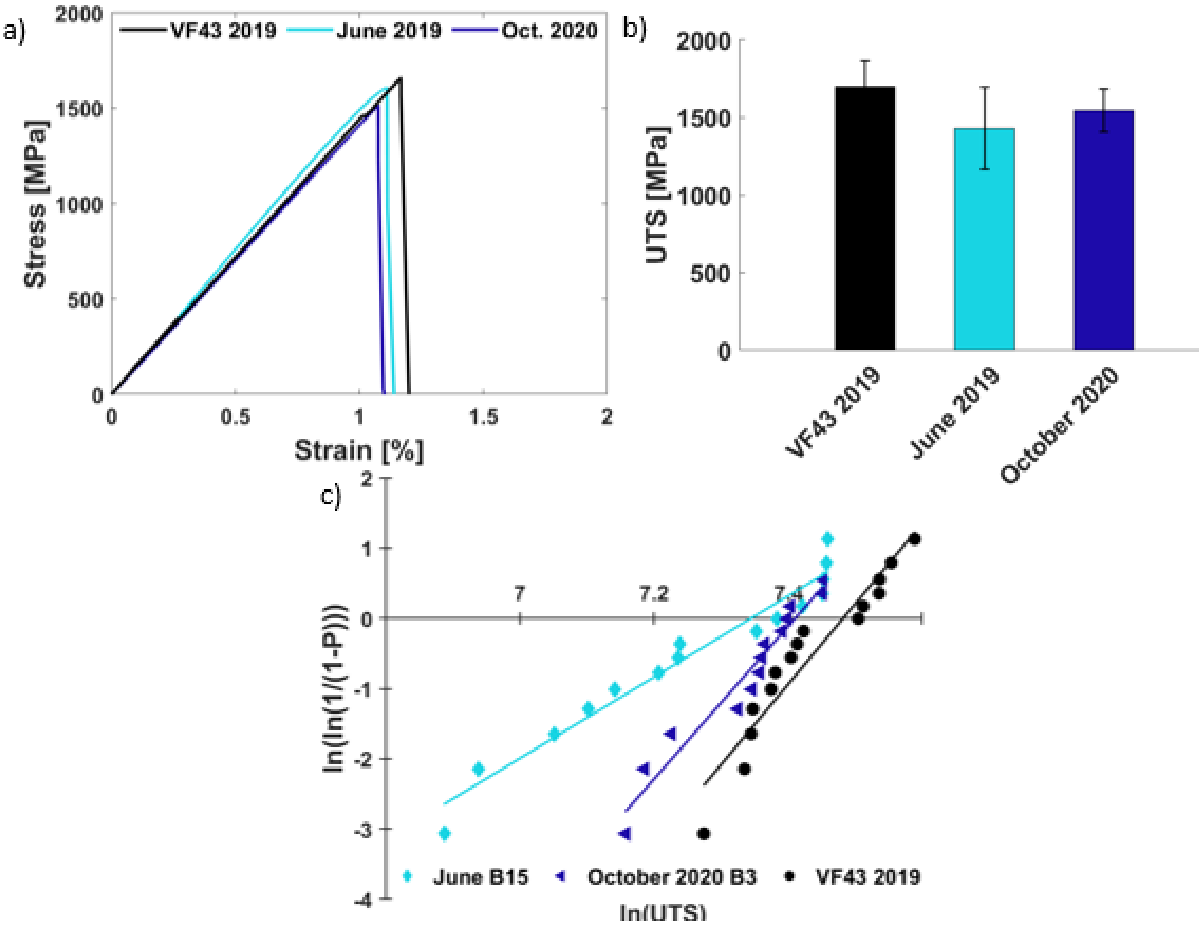

Figure 3.17. Representative stress-strain curves for printed samples. b) Average UTS comparison for printed samples with standard deviation. c) Weibull strength distribution in printed samples.

Table 3.4. Summary of mechanical results for printed specimens.

Batch	UTS [MPa] ± STD [MPa]	Weibull Modulus	Characteristic Life [MPa]
June 2019	1435 ± 265	5	1547
Oct. 2020	1630 ± 71	11	1652
VF43	1700 ± 165	11	1775

The Weibull modulus values of the printed samples in Table 3.3 are much lower than the values from the filaments evaluated in the unprinted condition. Hence, the variability in the mechanical behavior of the CCF/PPS material increases with the printing process. Based on early results suggesting that the printing process introduces defects in the filament during printing, there are potentially numerous contributing. The printing process can introduce many potential defects that should be explored to identify the root cause of strength degradation. Fortunately, the last batch of material produced by Toray (i.e. October 2020 batch) has significantly lower degree of variability in the ultimate tensile strength than the earlier manufactured batches.

3.3.3 Identifying Reduction in Strength Post-Deposition

An illustration describing the potential sources of strength reduction from the unprinted condition to the printed state in Figure 3.18. Damage is incurred within the composite filament at some points in the printing process. At present, it is unknown if the damage is matrix cracking, damage directly to the carbon fibers, or another mode. Regardless, this mechanical variance must be further investigated. To have a better understanding of the incremental contributions to filament damage and strength reduction, each operation in the print process was isolated. The strength distribution of the filament was assessed after each of the isolated components of the operation the filament from the June 2019 batch. A summary of the strength distribution is shown in Figure 3.18. The tensile strength of the as-received (unprinted) filament is 1885 MPa ± 130 MPa, which serves as a baseline for comparison of strength. When passed through the extruder only, consisting of a polyurethane roller and a rubber roller pressed together with the forces from a small spring, there was a 6.3% reduction in strength. When the material was passed through the extruder and nozzle (heated to 310 °C), the strength reduction was 7.4%. If the material bypassed the extruder and was pulled through the nozzle by the weight of a small object, there is a 6.1% reduction in strength with respect to the unprinted control.

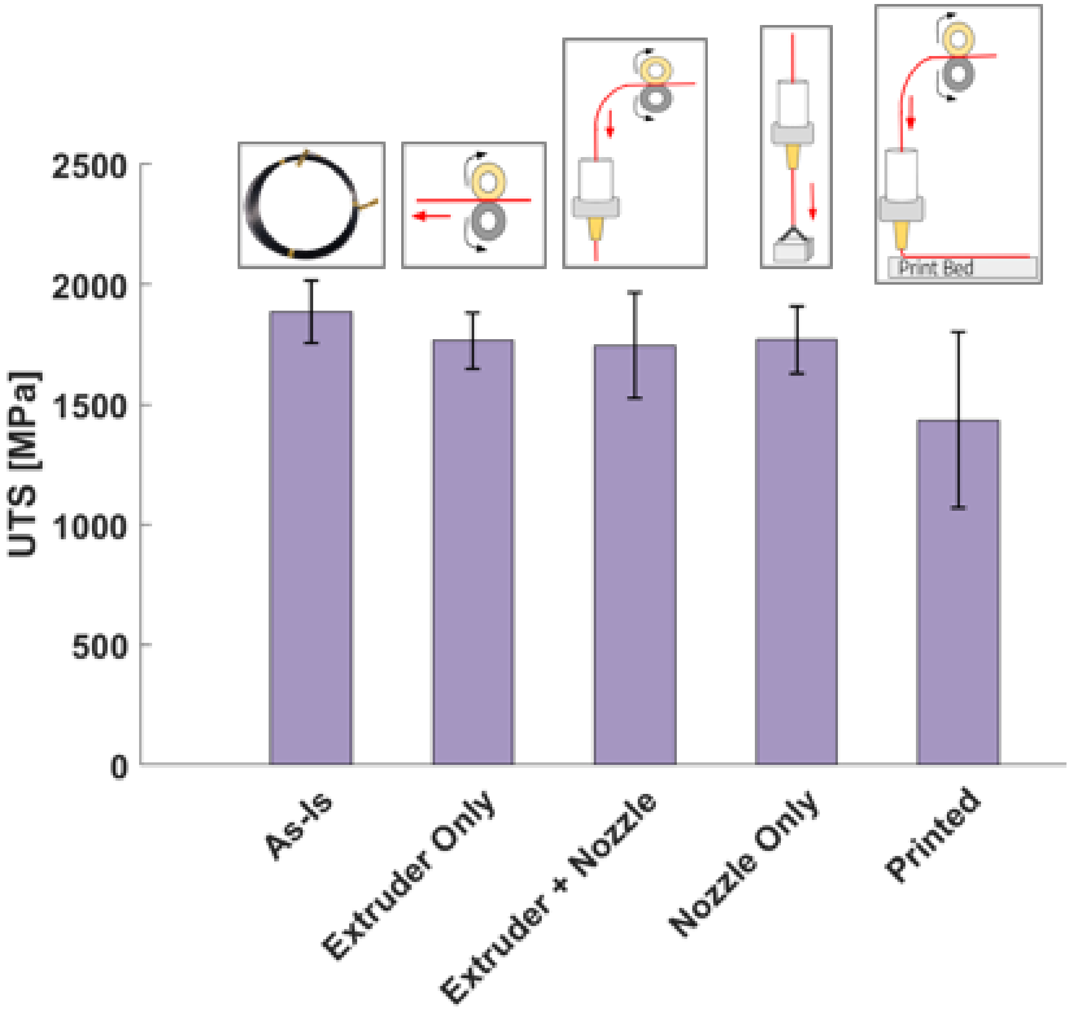

Figure 3.18. Average UTS with standard deviation for isolated print head components (depicted in diagrams).

This reduction in strength may not be considered substantial, but in an ideal process the filament would retain its strength of the unprinted condition. As evident in Figure 3.18, the largest reduction in strength occurred when the filament is printed onto the printer bed. The reduction in strength reaches nearly 25%. If the strength is predominately carried by the fibers and the contribution of the matrix is ignored, that reduction in strength implies that approximately 25% of the fibers are damaged in the printed condition, or approximately 1500 of the 6000 fiber tow.

Figure 3.19 shows results of fractography conducted on fractured filaments that were evaluated to failure after the steps shown in Figure 3.18. The extruder only, extruder and nozzle, and nozzle only samples all display a very similar failure mode, akin to that of the filament evaluated in the as- received condition. As all of the samples are from the June batch, heavy splaying is seen, which did not change while passing through the nozzle assembly. While new defects are apparently introduced during this process (deduced by the slight reduction in strength), the primary failure mode still appears to be related to twisting of the CF tow. After the filament is printed, the reduction in strength is 23.9%. Failure of the filament in this condition involves 3-10 cleanly split pieces, which is shown in Figure 3.19. The segmented failure morphology of the printed filament suggests that there are several isolated areas with defects that are being introduced to the filament during printing. This sample also displays a lateral split in part of the filament (upper side of Figure 3.19), presumably from a matrix dominated crack along the fiber/matrix interface.

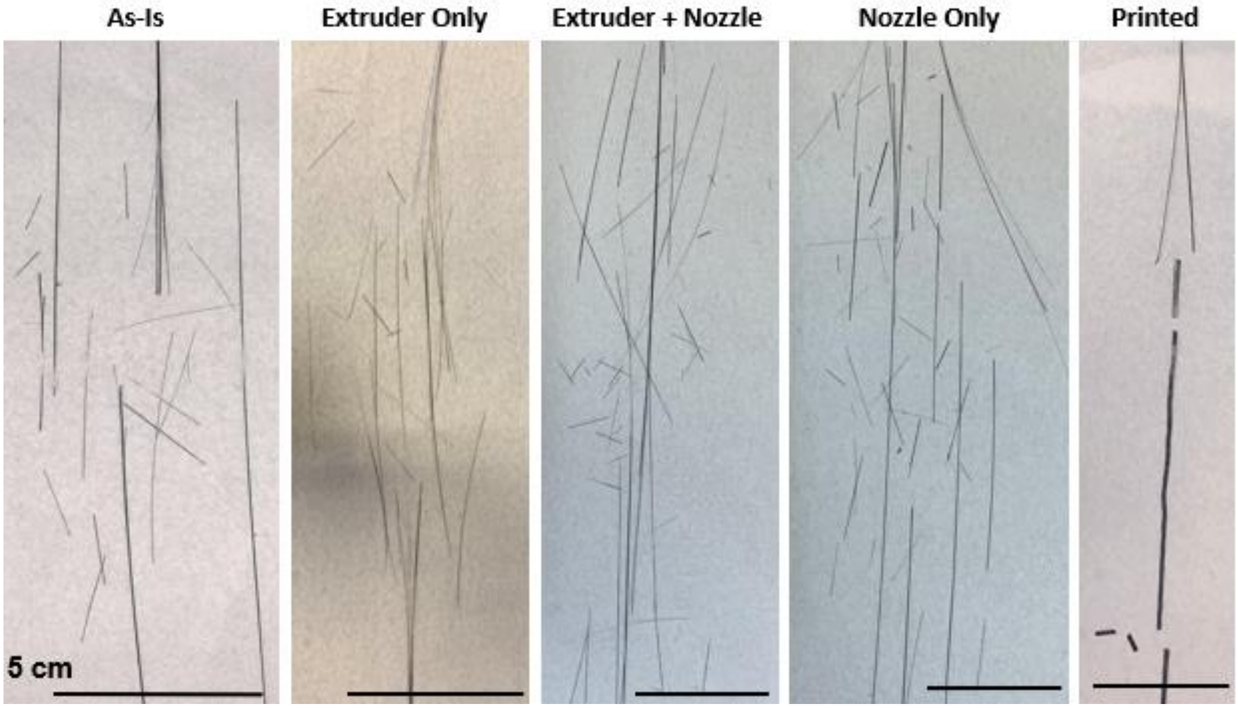

Figure 3.19. Representative images of fractured filament specimens after portions of the printing process.

The significant strength reduction occurs as a result of deposition of the filament onto the printer bed. The nozzle and the print bed are perfectly perpendicular and as such, the filament is deposited at a 90° angle. There is a chance that the radius of curvature or angle is too severe, and even at the elevated nozzle temperature, the carbon fibers undergoing a critical bending stress that causes fracture from damage introduced during extrusion or within the nozzle. A closer inspection of the filament via microscopy provides visual confirmation that some fibers are being damaged in the nozzle assembly as shown in Figure 3.20. When passed through the extruder only there were no surface defects evident. This implies that the contact pressure exerted between the extruder rollers and filament pinch the carbon fibers at the surface of the filament and cause defects. However, to confirm damage is introduced, a complementary method with higher spatial resolution would be needed to view the microstructure.

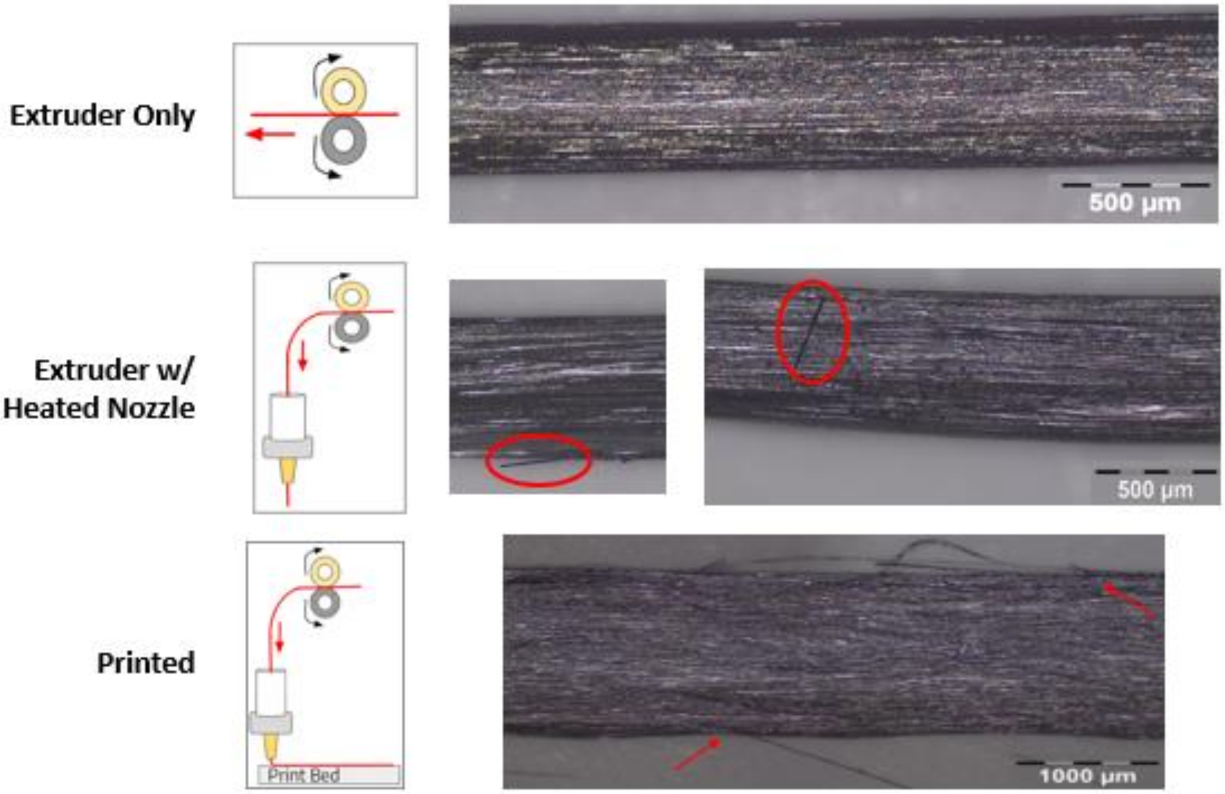

Figure 3.20. Optical microscopy of filament surface after undergoing the depicted process.

This discovery that the printed filaments exhibit significantly lower strength was an important accomplishment but can pose a significant hurdle to the commercialization of 3D printing of continuous fiber composites. Consumers will choose continuous fiber filaments for their superior mechanical response. Hence, if the printed material achieved substantially lower strength than expected, then the advantages of this material become tempered. Also, of note, the printed material exhibits significant variation in strength, with standard deviation of 365 MPa, and coefficient of variation of approximately 0.25. That reduction in strength raises a question: "can the mechanical response of FDM produced continuous fiber composites be predicted?". Clearly, more physical testing is needed to understand the root cause of failures and to engineer solutions that mitigate the reduction in strength.

3.4 Printing Productivity

In addition to the DOE and mechanical analysis, the printing productivity was also investigated. Consumers will often want to know how fast parts can be produced and what quality should be expected. One of the main benefits of AM is the ability to rapidly produce parts. However, there are some speed limitations when printing continuous fiber filaments. For example, the flow rate must compliment the printing speed such that the rate of filament extrusion matches the speed of the printer movements. Continuous fiber filaments require that the extrusion to deposition ratio is 1:1, as there is negligible elasticity or plasticity in the CF tow. This is not an issue in printing with unreinforced polymer filaments. Thus, the flow rate and print speed are heavily interdependent and as the desired print speed is increased the flow rate should be increased to accommodate that.

To illustrate VF50's printability, an array of samples was printed varying the nozzle temperature and print speed over the range of possible parametric settings; the flow rate was increased accordingly. Figure 3.21 displays a productivity map showing the printability as a function of the printed material quality. For reference, PLA is printed at a rate of roughly 3600 mm/min, and more elastic filaments such as TPU are printed around 1200 mm/min. In comparison, the VF50 performs best at a much lower rate, between 250-600 mm/min using the Prusa printer. One of the primary limitations noticed in this effort was adhesion of the filament to the build plate. As there is less polymer present in this composite filament when compared to an unfilled filament, the speed has to be slow enough to allow adequate time for the sparse PPS to adhere to the printer bed or previously deposited layer surfaces. As evident from the printability map, this filament is best printed at around 400 mm/minute at a nozzle temperature of 340 °C to 350 °C. Samples printed at these conditions exhibit a smooth surface with no visible defects. Also evident, this filament should not be printed below 310 °C, as the PPS is not in a sufficiently melted state to flow and adhere to the print bed. At faster print speeds the samples experienced warping along the edge where the filament turns to start to the next row. The faster speeds hamper the quality of adhesion and tension in the fiber reinforcement eventually pulls the filament enough to cause warping during cooling.

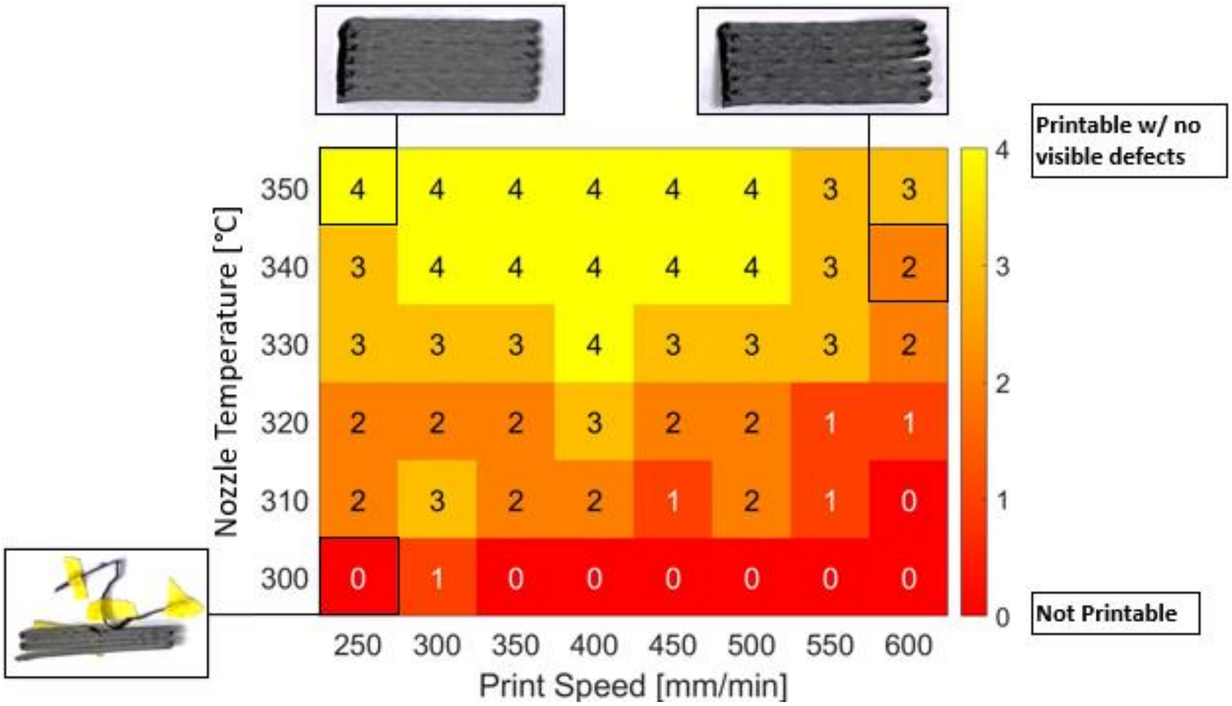

	250	300	350	400	450	500	550	600
350	4	4	4	4	4	4	3	3
340	3	4	4	4	4	4	3	2
330	3	3	3	4	3	3	3	2
320	2	2	2	3	2	2	1	1
310	2	3	2	2	1	2	1	0
300	0	1	0	0	0	0	0	0

Figure 3.21. A productivity map describing the quality of printed filament in terms of the two most influential process parameters. The flow rate was increased from 58-61% as print speed increased to maintain the balance of extruded and deposited material. Examples of printed samples are also shown.

Chapter 4 – Discussion

In this investigation a newly developed high volume fraction composite filament of CCF/PPS was acquired from Toray Inc and an experimental evaluation of the printability and mechanical properties was conducted. Intended for applications in the aerospace industry, this material system could ignite new focused on AM of high strength composites. Although a prototype, this CCF/PPS system achieved tensile strengths that exceed 2 GPa, which exceeds the reported strengths of any FDM filaments. In addition, the preliminary prints were found to be dimensionally accurate and with a visibly smooth surface. These results are promising and provide some optimism for future commercial applications

Despite the many positive qualities encountered in printing of the new CCF/PPS filament, there are several obstacles to overcome before this filament can be considered for widespread application, especially in aerospace. Specifically, as highlighted by the reduction in strength and details obtained from microscopy performed on the filament surface, it appears that some carbon fibers incur damage during printing. As carbon fibers serve as the principal load bearing members in tension, fiber damage is highly detrimental. Secondly, while the bulk of this study focused on monolayer specimens, some multi-layer samples were printed with varying degrees of layer adhesion, and with increasing layer number. As more layers are printed, the degree of interlayer adhesion becomes worse, which could lead to a low interlayer shear and tensile strength. As industrial components are generally over 10 layers (~2 mm using average layer thickness of 0.2 mm), poor layer adhesion in as few as five layers is a critical concern. Such defects could reduce interest in these high fiber volume fraction filaments. The following chapter explores the observed barriers to producing flaw-free 3D printed components with a high volume fraction composite filament.

4.1 Ideal Print Path

The following activities utilized a custom MATLAB script to write GCODE with a continuous tool/print path. Since a basic desktop printer is used, the device did not have a method of cutting the filament during printing, so transitions between layers or specimen features require interruption of the process. In addition, no filament retraction is used. For example, Figure 4.1a shows a sample with a 0°/90° cross hatch 2-layer pattern. When inspecting the turning points of the filament as highlighted in (Figure 4.1b) it can be noticed that the filament undergoes twisting when being placed around curves. The more turns that the printer completes in succession, the larger degree of torsion that the filament is subjected to.

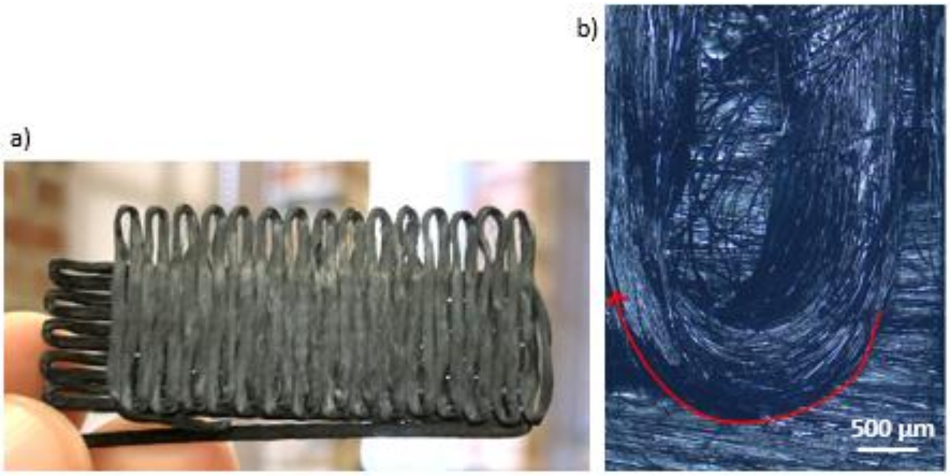

Figure 4.1. Printing of laminates. a) 2-layer VF50 printed sample with 0°/90° fiber orientations with b) a magnified view of a turn, showing some filament twisting and loose fibers.

In some cases where twisting occurred, residual tension led to poor deposition and critical print failure. Tight placement of the filament is a key advantage of FDM, and if basic turns and curves cause the generation of more defects in using the VF50 material that reduces its overall quality, the print process must be addressed. The limitations of the system are an important design consideration for printing more complex specimens. One viable option is that there are experimental printers that feature rotating nozzle heads (Raney, et al., 2018). An extension like this might be able to counteract some of the filament twisting leading to more intricate design without loss of performance. In addition, in Figure 4.1b, it should be pointed out that strands (likely consisting of small bundles of carbon fibers surrounded by PPS) can be seen isolated from the main filament matrix (within center of turning point). These outlying fiber groups become more susceptible to damage and potentially exposed the printed filament to further reductions in strength.

Not only is filament twisting an important consideration for specimen curvature limitations, but the influence of print path on the microstructure must also be considered. To address that concern, a small pilot experiment was conducted with MF filament to illustrate the internal movement of carbon fibers during deposition. It was previously mentioned that an ideal microstructure for this filament has an even dispersion of fibers with minimal clustering. Thus, when printing a circle with a radius of curvature of 15 mm (Figure 4.2a), an ideal microstructure should have a regular shape and fiber distribution. Figure 4.2b displays a misshapen cross-section (a rectangular cross-section is expected) with fibers pulled towards the upper corner of the inside of the print path. There is a large clustering of fibers at the surface with matrix-rich regions on the bottom and center of the cross-section as evident in this figure. Even at 50% completion of the circular path (where the cross-section is taken for analysis), the print head is dragging the carbon fibers towards the inside edge of the deposition. There is a clear correlation between the specimen design features and the resulting microstructure. A method must be implemented to minimize fiber clustering and tension in the tow from the print head that will ultimately cause fiber misplacement and reduction in the overall quality.

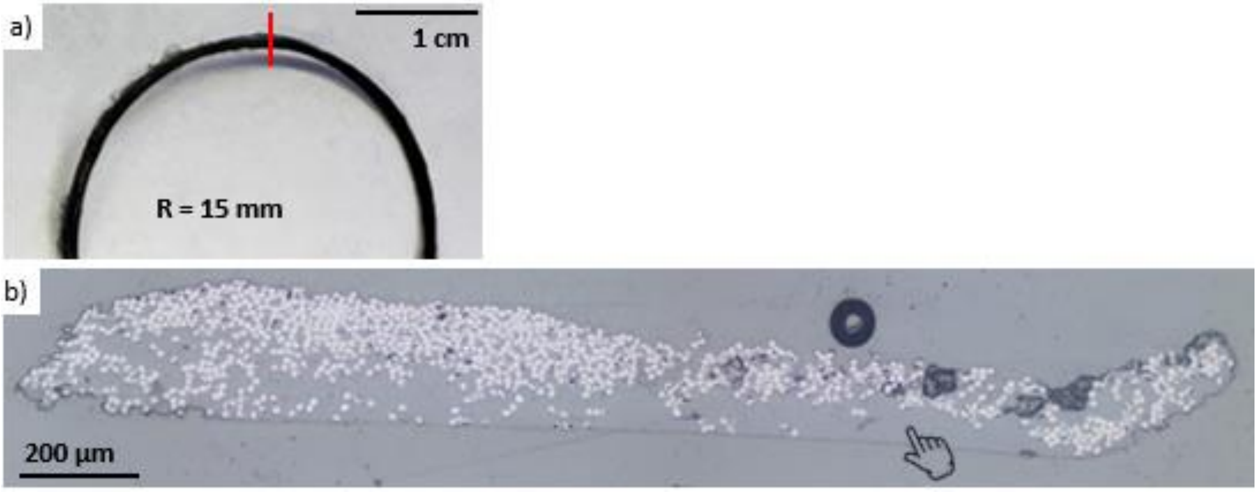

Figure 4.2. Microstructure variations with printing path in MF filament. a) A portion of a printed circle with a radius of 15 mm which was then cut at the red line revealing b) an unbalanced printed microstructure (left edge is inner side of sample). Note the matrix-rich area highlighted by the pointer.

Furthermore, five simple shapes were designed to reflect the VF50 printability with respect to angular features. These shapes were printed using conditions known to result in higher quality printed samples and within range of optimal parameter levels from the productivity map. Figure 4.3 shows the printed shapes along with a more highly magnified view of the defects present. Overall, the filament is able to conform to acute angles very easily, although some fiber twisting is noticed. It is unclear whether the fibers are able to be deposited within the interior regions of these angles without becoming weakened or damaged due to the bending. The filament has difficulties printing features that involve obtuse angles such as those in the pentagon (108°). Similar difficulties are seen when printing circles with larger radii of curvature. Tension within the CF tow must be maintained during printing. If a subsequent deposition line is laid in an opposing direction, the weak adhesion forces keeping the filament secured to the print are overcome and the sample will prematurely lift off the print bed.

A region of the printed square in Figure 4.3c shows two continuous and concentric deposition lines, where the outer line was printed first. A significant amount of fiber waviness is evident in the outer line, as well as on the left side of the square (Figure 4.3a). In addition, there is a large gap at the corner. Ideally, there would be no gaps and just the right amount of overlap to ensure a strong interlayer bond is achieved. Perhaps the flow rate here was not optimized for this geometry and the print path should be closer together at the turning point; fine tuning of the process parameters could potentially diminish such defects. Nevertheless, in conceptualizing the next generation of components produced using a high volume fraction CCF/PPS filament, one can appreciate that each geometry will have special considerations based on the features and tool path. For example, in some aerospace application the components will require open holes to accommodate mechanical fasteners. Continuous fiber designs around these holes are of special interest (Chuaqui, et al., 2021; Shafighfard, et al., 2019; Su, et al., 2020) as well as optimizing the fiber reinforcement these areas of stress concentration.

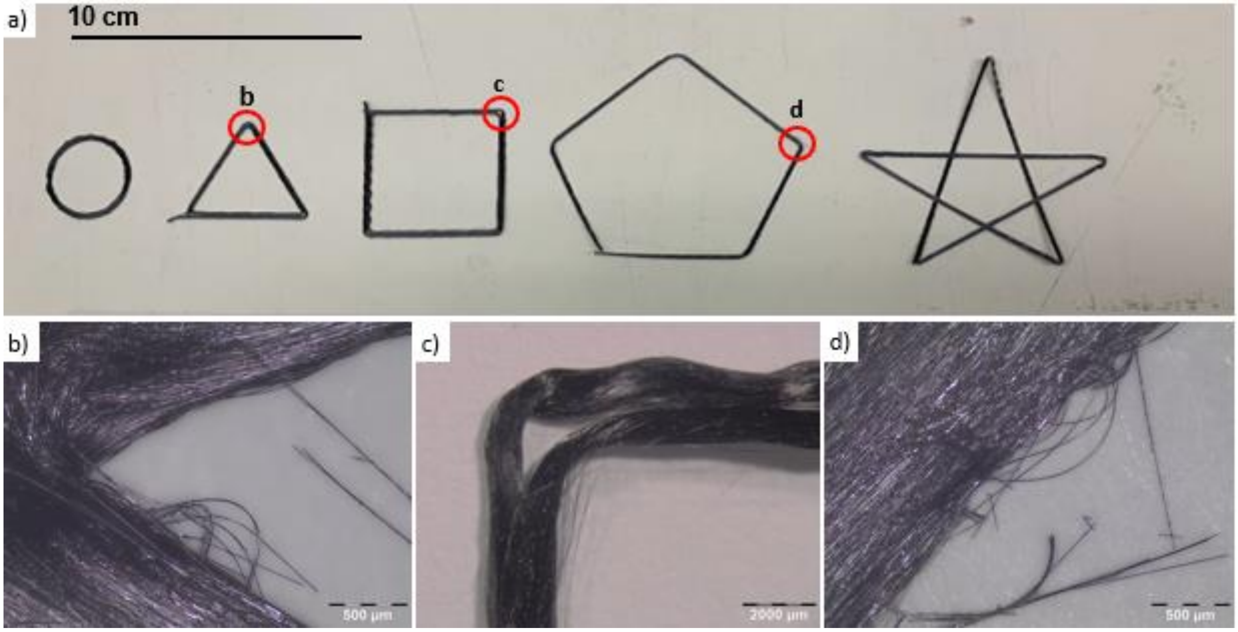

Figure 4.3 Exploring the printability of the VF50 CCF/PPS. a) Outline of basic shapes to illustrate printability at different angles, b) close-up showing two groups of broken fibers, c) close-up displaying fiber waviness in the outer row and broken fibers in the inner row, d) close-up showing many broken surface fibers.

Common to each of the explored geometries, there was evidence of damage to the surface of the carbon fibers. Defects related to features of the specific shapes were presented in Figures 4.3b-d. The small slivers of filament consist of small clusters of broken CFs, but should be further investigated under SEM. The surface defects of the filaments can be placed in two categories; i) separated from the main filament body and bowed out but not broken, and ii) fibers that have been completely fractured. While Figure 3.20 identified the particular step in the printing process that resulted in the greatest loss of strength and most apparent damage, the exact causes of the fiber separation and fracture are unknown. One possible explanation is from internal scratches within the nozzle, which impart damage onto the filament during extrusion. Ideally, a nozzle that is used for printing of carbon fiber-based filaments is made of hardened steel. However, in this experiment a brass nozzle was used due to availability. A hardened steel nozzle could increase the resistance to scoring and maintain a low surface roughness that could improve the printed specimen quality. Another explanation could be that a small degree of buckling of the filament occurs as it is passes through the nozzle assembly. If the extrusion rate is a little fast with respect to the print speed, the filament could get choked within the confines of the nozzle assembly, leading to cracks within the filament that become exacerbated during deposition onto the print bed. Regardless, broken fibers on the filament surface are an obvious contributor to reduced material strength and the root cause of that damage should be identified and eliminated.

4.2 Layer Adhesion and Possible Thermal Treatments

In general, the primary focus of this investigation was the basic parametric contributions to the printed material quality and as a result, monolayer samples were used throughout this investigation. As 3D printed specimens are rarely just one layer, the printing behavior of high volume fraction composites with multiple layers is the logical next evolution in this investigation. The simple rectangular geometry utilized through this work was printed in multiple layers and is demonstrated in Figure 4.4. Determined from the DOE in printing with VF50, the Z-height is a primary contributor to the printed surface roughness and adhesion of the material to the print bed. In addition, as a model is built up in the Z-direction, Z-height becomes critical in applying pressure to encourage the PPS to bond to the previous layers.

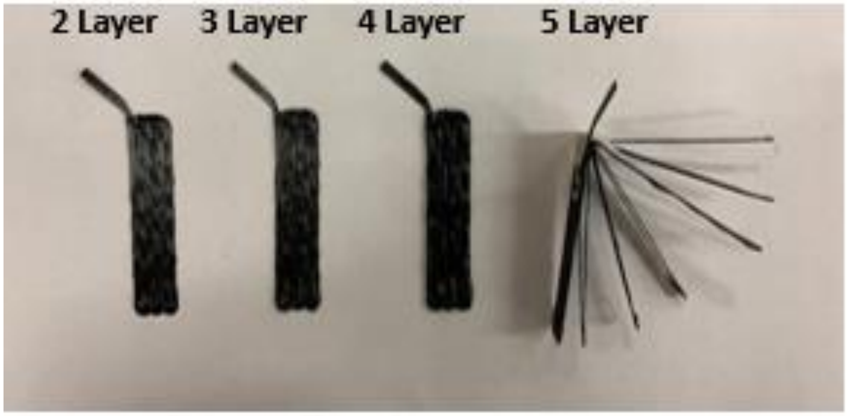

Figure 4.4. Multilayer samples printed with the VF50 CCF/PPS. Each layer is the same 0° orientation. Adhesion between layers becomes poor after the 5th layer.

It is hypothesized that a number of factors contribute to the poor layer adhesion. After the 5th layer, it became more challenging to keep the layers contained. Without applying direct pressure, the layers tended to spring apart from the end in which the layers turned to complete the next layer. The elastic strain energy in the fibers that results from bending of the filament is the driving force for this “springback” in the consolidated filament. The desktop 3D printers utilized in this investigation do not have an enclosed build space. As such, the specimens are subjected to ambient room conditions during a build. The print bed is heated to 90 °C, which provides some heat to the initial deposited layer. As continuous fiber filaments must be printed at a slower rate, the creation of each layer can take several minutes depending on part size. That time allows extra cooling and facilitates a significant amount of heat loss from the system. As the number of layers increases, the new deposition is farther away from the maintained temperature of the heated bed and there is more time for the specimen to cool. The addition of an enclosed build space could elevate the ambient temperature and keep the PPS in a softened state throughout the whole structure. However, this approach might work for controlled experiments in a laboratory but may be difficult to achieve in industrial practice.

A colleague involved in this work has introduced a post-processing step that follows printing of the VF50, in which a multi-layer part is subjected to heat and compaction to consolidate the layers. He noted that interlayer porosity is detrimental to strength and this this post-processing and increased the interlayer strength considerable. Ideally, this process would be concurrent with the printing process to save time and energy. Similarly, Arevo utilizes a compaction roller during their DED process as discussed in Section 1.3. Therefore, a post-printing heat treatment like hot isostatic pressing could be a key solution to achieve the desired part density and strength. A heat treatment could allow the PPS time to bond between adjacent layers, settle voids, and further polymerize (enhancing PPS crystallinity and strength). Initial heat treatments (100-minute dwell at 200 °C or 240 °C) were conducted on a monolayer printed VF50 specimen (printed with nozzle temp of 310 °C). Results showed an increase in crystallinity from the untreated printed CCF/PPS from 35.2% to 40.1%. Further crystallinity increases might also be seen if a lower VF filament is used. The influence of crystallinity to the mechanical strength must be further investigated. Nevertheless, requiring a post-processing step to achieve the desired strength is not desirable as that is the drawback of using thermosetting composites and currently serves as the impetus for adopting thermoplastic composites in aerospace.

The volume fraction of polymer matrix is also influential to layer adhesion. The PPS of the filament is the singular source of adhesion between layers and will be the weakest component of the system. With higher volume fraction filaments, such as in printing of the VF50, there is less initial matrix. The MF filament was successfully printed with 5+ layers with excellent surface finish and minimal visible voids or defects. A cross section of a 5-layer rectangular beam produced with the MF filament is shown in Figure 4.5. While there are areas with poor CF dispersion, there are no significant separations between layers. There are some voids that are evident, but these are hard to eliminate entirely with any polymer composite (Mehdikhani, et al., 2018).

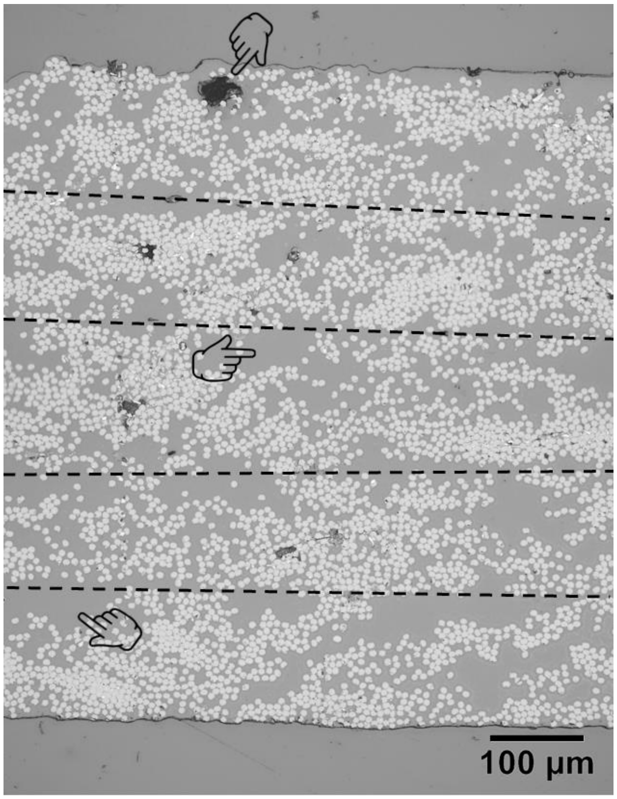

Figure 4.5. A cross-section of a beam specimen printed with five layers of MF filament. The dotted line shows the suspected layer boundaries, with voids and matrix rich regions pointed out.

4.3 Towards Design of an Accessible Continuous Fiber Printer

As highlighted in this chapter, there are a number of concerns in printing the CCF/PPS VF50 filament and aspects of the printed microstructure of performance that were found to be less than ideal. The use of a common research grade FDM printer may have resulted in samples with reduced mechanical strength and poor layer adhesion, and these concerns would increase in larger designs. Nevertheless, the results show tremendous potential in terms of the material printability and the mechanical properties that can be achieved. Therefore, there would be substantial value to continue advancing the material and optimizing this process. If these advancements can be accomplished on an open-source FDM system, it will provide the world access to this advanced material system, which can further stimulate research efforts. The creation of an affordable system that can reliably produce high-quality thermoplastic composites would be attractive to many industries.

It is believed that a few modifications to the basic printer design can help facilitate the best possible printing of VF50 and other high VF filaments. For instance, the print head is perpendicular to the build plate, and it is not yet known if forcing the filament out at this angle is cause for the fiber damage and reduction in strength. If the entire print head and/or nozzle assembly were tilted to have an acute angle on the leading edge (with the X-axis belt remaining horizontal through the head), the filament could be deposited an obtuse angle rather than at 90°. A more gradual angle might alleviate the bending stresses at the site of deposition. There would be some new concerns regarding the nozzle Z-height, but these can be addressed, as necessary. Another adjustment to the nozzle that could provide additional value is to address fiber twisting. If the nozzle also enabled programmable rotation or guided rotation, a slow rotation during curves could counteract the filaments tendency to twist. Laying a filament with a smooth fiber tow will undoubtedly improve mechanical properties as there will be less potential fiber damage.

As previous mentioned, an enclosed environment could serve to maintain the specimen at an elevated temperature during its build, allowing the PPS additional time to bond together. This could be accomplished with minimal cost in the form of a basic acrylic box that encloses the build space. The external power unit and other essential electronics would be excluded to prevent overheating of the build chamber. An enclosed and controlled environment within its own heat source could circumvent the need for post-printing thermal treatments as the printed specimens would undergo slower cooling, diminishing the enthalpy of cold crystallization and result in greater crystallinity. Not only would this hopefully strengthen the bonds between the layers but also enhance the overall printed filament strength. Additionally, the spring forces that maintain the contact force of the extruder rollers could be adjusted for this application. A decrease in the clamping force that is administered by the extruder would be expected to reduce the fiber damage assuming damage is occurring during this step of the process. The aforementioned print process modifications are logical starting points for further advancements and optimization of FDM of continuous fiber composites.

Chapter 5 – Conclusions and Future Work

5.1 Conclusions

In this thesis, a novel composite filament with high volume fraction carbon fibers developed by Toray Industries for Fused Deposition Modeling (FDM) was evaluated. The primary objectives were to characterize the general physical and mechanical properties of the material system, compare those to existing commercial materials as well as explore the filament printability. It is anticipated that this material could advance the current state of the art in Additive Manufacturing (AM) of high strength composites and be employed in the fabrication of composite structure for aerospace and beyond.

The investigation involved a comparison of the thermal and mechanical properties of the Toray material system, which consisted of Continuous Carbon Fibers (CCF) and a Polyphenylene (PPS) matrix, with fiber volume fraction (VF) ranging between 35-50%. The material and its printability were compared with a continuous carbon fiber reinforced polyamide distributed by Markforged (CCF/PA) with approximately, ~28% VF fibers. Using image analysis, it was shown that the fiber distribution of the CCF/PPS is significantly more uniform than that of the MF system. The higher fiber VF of the Toray filaments led to higher tensile strength, from 1485 MPa (MF) to 1945 MPa for the VF50 of Toray. Results obtained from TGA and DSC showed that the PPS began to decompose at just under 500 °C, and that the printed crystallinity of the VF50 was approximately 35.5%. The screening DOE revealed that nozzle temperature, print speed, flow rate, and Z-height were the more significant parameters that contributed to the printed specimen quality.

Results from a Design of Experiments (DOE) showed that the printed surface roughness was primarily dependent on the Z-height and was minimized using a Z-height of 0.2 mm. The fiber placement, dimensional accuracy, and porosity of the printed CCF/PPS was dependent on more complex interactions of the printing parameters, which suggests that control of the microstructure is challenging. Defining acceptable tolerances for the printed quality will be an important step to moving forward.

The mechanical properties of the filament after printing and the contribution of various aspects of the extrusion and melting process were explored. Given the geometry of the designed tensile grips, samples groups were produced that involved isolating distinct components of the nozzle assembly and then tested in tension. When passing through either the extruder or nozzle, or both, the UTS of the filament decreased by 6.1 to 7.4%, whereas after deposition onto the print bed the strength was reduced by an average of approximately 24% and involved a large amount of variability. An appreciable amount of damage to the filament surface was also seen through optical microscopy. Although the majority of damage causing reduction in strength came after deposition onto the print bed, defects introduced during the extrusion process could serve as the root cause of reduced strength.

Finally, a determination of the optimal printing conditions for the FDM process and printing of the VF50 system was performed. Through a printing process productivity matrix, the best quality of printed material was produced at 345 °C and ~200 mm/min. Various feature geometries were printed at these conditions and the quality was investigated. Circular print paths significantly influenced the microstructure and CF placement. Furthermore, more substantial damage to the filament surface was observed when printing at a variety of angles. Other printing defects include fiber waviness and gaps between adjacent deposited filaments. Preliminary printing of the VF50also showed that the interfacial layer adhesion failed after deposition of 5 layers. This will lead to a very low interlayer shear strength and must be overcome for this process to have commercial viability.

In summary, the results advance our understanding and capability for AM of high volume fraction composite structures. As evident by the reduction in strength after printing, and the visualization of surface defects, there are several difficulties that first must be addressed for FDM of continuous fiber composites. Yet, the research conducted demonstrates a promising future of applied FDM composites. The work done will lead to enhanced filament and printing systems. These contributions to the field of high-performance composites will help spearhead the push for certified thermoplastic composites in industry.

5.2 Future Work

While the investigations described within this thesis provided new understanding of the printing process and its effects on the strength of continuous fiber composites with high fiber VF, there are many exciting avenues of further research. The collaboration between the UW and Toray is ongoing, and the Arola Group continues to work with them in optimizing a CCF/PPS material for FDM. Additional efforts will focus on increasing the PPS on the exterior of the filament in an effort to reduce potential CF damage during extrusion. The recommended printer modifications should be implemented to provide the best opportunity for printing this material system with minimal defects. There is substantial work that could be focused on fine-tuning the 3D printer for continuous fiber filaments. To strengthen this effort, an additional printing system should be included in the investigation. For example, the Mark 2 printer by Markforged is of particular interest, as it is readily available for use at the UW. If the damage that was observed after printing with the Prusa printer also occurs with the Markforged printer, the community of researchers in this area should be alerted of this fundamental flaw in the FDM process what applied to continuous fiber systems.

In addition to aerospace applications, there are applications to marine settings that should also be explored. The thermoplastic PPS could also provide good resistance to degradation from sea water, as it has the best chemical resistance of thermoplastics [ref?]. In addition, the fundamental knowledge obtained in investigating the CCF/PPS system could be applied to a large number of polymer/fiber combinations. An optimized FDM process could then be developed to achieve printing of many target geometries. Material systems could range from synthetic and highly engineered, to more bio-based systems such as hemp, jute fibers, and cellulose based composites. Not only could experimental systems have a matrix and continuous microscale fiber, but nanoscale additives could be added to enhance interfacial strength, filler dispersion, and environmental degradation. Additives could include nanoparticles within the matrix, surface treatments to the fibers or both.

Lastly, if continuous fiber composites are successfully developed for FDM, they could be used to mimic natural biological composite microstructures. Osteons in bone, the decussated enamel patterns in teeth, and the brick-and-mortar structure of nacre are examples of hierarchical microstructures of biological structure materials that are capable of providing incredible strength and resistance to fracture. An optimized continuous fiber system and robust approach for printing could enable the realization of biomimetic materials that emulate many of these natural systems, which are presently not possible to manufacture with traditional methods. One of the most exciting aspects of AM, is pushing the manufacturing boundary beyond what is presently possible. This is an especially exciting field of research that will produce the next generation of composite structures.

References

Ashby, M., 2008. *The CES EduPack Database of Natural and Man-Made Materials,* s.l.: Engineering Department, Cambridge University.

ASTM D3039, 2017. *Standard Test Method for Tensile Properties of Polymer Matrix Composite Materials,* West Conshokocken: ASTM International.

ASTM D628-14, 2014. *Standard Test Method for Tensile Properties of Plastics,* West Conshohocken: ASTM International.

ASTM Standard F2792, 2013. *Standard Terminology for Additive Manufacturing Technologies,* West Conshohocken, PA: ASTM International.

Awais, H. et al., 2021. Environmental benign natural fibre reinforced thermoplastic composites: A review. *Composites Part C: Open Access,* Volume 4.

Bachmann, J., Hidalgo, C. & Bricout, S., 2017. Environmental analysis of innovative sustainable composites with potential use in aviation sector—A life cycle assessment review. *Science China Technological Sciences,* Volume 60.

Bhuvanesh Kumar, M. & Sathiya, P., 2021. Methods and materials for additive manufacturing: A critical review on advancements and challenges. *Thin-Walled Structures,* Volume 159.

Blok, L., Longana, M., Yu, H. & Woods, B., 2018. An investigation into 3D printing of fibre reinforced thermoplastic composites. *Additive Manufacturing,* Volume 22, pp. 176-186.

Brady, D., 1976. The crystallinity of poly(phenylene sulfide) and its effect on polymer properties. *Journal of Applied Polymer Science,* 20(9), pp. 2541-2551.

Brenken, B. et al., 2018. Fused filament fabrication of fiber-reinforced polymers: A Review. *Additive Manufacturing,* Volume 21, pp. 1-16.

Callister, W. D. J. & Rethwisch, D. G., 2015. *Fundamentals of Materials Science and Engineering: An Integrated Approach.* 5th ed. s.l.:Wiley.

Chen, J., Fu, K. & Li, Y., 2021. Understanding processing parameter effects for carbon fibre reinforced thermoplastic composites manufactured by laser-assisted automated fibre placement (AFP). *Composites Part A: Applied Science and Manufacturing,* Volume 140.

Chockalingam, K., Jawahar, N. & Praveen, J., 2016. Enhancement of Anisotropic Strength of Fused Deposited ABS Parts by Genetic Algorithm. *Materials and Manufacturing Processes,* 31(15), pp. 2001-2010.

Chuaqui, T. et al., 2021. Effects of ply angle and blocking on open-hole tensile strength of composite laminates: A design and certification perspective. *Composites Part B: Engineering,* Volume 207.

CSIR - National Aerospace Laboratories, 2018. *Resin Transfer Moulding Processes.* [Online] Available at: https://www.nal.res.in/en/techniques/resin-transfer-moulding-processes [Accessed 11 2 2021].

Der Klift, F. et al., 2016. 3D Printing of Continuous Carbon Fibre Reinforced Thermo-Plastic (CFRTP) Tensile Test Specimens. *Open Journal of Composite Materials,* 6(1), pp. 18-27.

Dietrich, D., Kenworthy, M. & Cudney, E., 2019. *Additive Manufacturing Change Management.* 1st ed. Boca Raton: CRC Press.

Ferreira, R., Amatte, I., T, D. & Bürger, D., 2017. Experimental characterization and micrography of 3D printed PLA and PLA reinforced with short carbon fibers. *Composites Part B: Engineering,* Volume 124, pp. 88-100.

Fischtziur, E., 2015. *'Grand-scale' autoclave for Boeing's biggest wings nears completion.* [Online]
Available at: https://www.boeing.com/company/about-bca/washington/grand-scale-autoclave-for-boeing-s-biggest-wings-nears-completion-06-16-2015.page
[Accessed 10 2 2021].

Garzon-Hernandez, S., Garcia-Gonzalez, D., Jérusalem, A. & Arias, S., 2020. Design of FDM 3D printed polymers: An experimental-modelling methodology for the prediction of mechanical properties. *Materials & Design,* Volume 188.

Geng, P. et al., 2018. Effect of Thermal Processing and Heat Treatment Condition on 3D Printing PPS Properties. *Polymers,* 10(8).

Gibson, I., Rosin, D. & Strucker, B., 2015. *Additive Manufacturing Technologies.* 2nd ed. New York: Springer.

Gunasekaran, K. et al., 2020. Investigation of mechanical properties of PLA printed materials under varying infill density. *Materials Today: Proceedings.*

Hajikazemi, M., McCartney, L. & Van Paepegem, W., 2020. Matrix cracking initiation, propagation and laminate failure in multiple plies of general symmetric composite laminates. *Composites Part A: Applied Science and Manufacturing,* Volume 136.

Hou, Z., Tian, X., Zhang, J. & D, L., 2018. 3D printed continuous fibre reinforced composite corrugated structure. *Composite Structures,* Volume 184, pp. 1005-1010.

Hsissou, R. et al., 2021. Polymer composite materials: A comprehensive review. *Composite Structures,* Volume 262.

Irving, P. & Soutis, C., 2020. *Polymer Composites in the Aerospace Industry.* 2nd ed. s.l.:Woodhead Publishing.

Keyence Corporation, 2020. *Area Roughness Parameters.* [Online]
Available at:
https://www.keyence.com/ss/products/microscope/roughness/surface/parameters.jsp
[Accessed 10 January 2021].

Klosterman, D., 2018. *Development of a Simple Lab-Scale Vacuum Assisted Resin Transfer Molding (VARTM) Process.* Dallas, CAMX - The Composites and Advanced Materials Expo.

Kokkinis, D., Schaffner, M. & Studart, A., 2015. Multimaterial magnetically assisted 3D printing of composite materials. *Nature Communications,* 6(1).

Lee, T., Boey, F. & Khor, K., 1995. On the determination of polymer crystallinity for a thermoplastic PPS composite by thermal analysis. *Composites Science and Technology,* 53(3), pp. 259-274.

Li, N., Li, Y. & Liu, S., 2016. Rapid prototyping of continuous carbon fiber reinforced polylactic acid composites by 3D printing. *Journal of Materials Processing Technology,* Volume 238, pp. 218-225.

Liu, S. & Shin, Y., 2019. Additive manufacturing of Ti6Al4V alloy: A review. *Materials and Design,* Volume 164.

Lubin, G., 1982. *Handbook of Composites.* s.l.:Springer US.

Maemura, E., Cakmak, M. & White, J., 1989. Characterization of crystallinity, orientation, and mechanical properties in biaxially stretched poly(p-phenylene sulfide) films. *Polymer Engineering & Science,* 29(2), pp. 140-150.

Mahajan, C. & Cormier, D., 2015. *3D Printing of Carbon Fiber Composites With Preferentially Aligned Fibers*, s.l.: Institute of Industrial and Systems Engineers.

Marsh, G., 2007. Airbus takes on Boeing with reinforced plastic A350 XWB. *Reinforced Plastics,* 51(11), pp. 26-29.

Matsuzaki, R. et al., 2016. Three-dimensional printing of continuous-fiber composites by in-nozzle impregnation. *Scientific Reports,* 6(1).

Mehdikhani, M., Gorbatikh, L., Verpoest, I. & Lomov, S., 2018. Voids in fiber-reinforced polymer composites: A review on their formation, characteristics, and effects on mechanical performance. *Journal of Composite Materials,* 53(12), pp. 1579-1669.

Naranjo-Lozada, J. et al., 2019. Tensile properties and failure behavior of chopped and continuous carbon fiber composites produced by additive manufacturing. *Additive Manufacturing,* Volume 26, pp. 227-241.

Ning, F. et al., 2015. Additive Manufacturing of carbon fiber reingorced thermoplastic composites using fused deposition modelling. *Composites Part B: Engineering,* Volume 80, pp. 369-378.

Parandoush, P. & Lin, D., 2017. A Review on Additive Manufacturing of Polymer-Fiber Composites. *Composite Structures,* Volume 182, pp. 36-53.

Raney, J. et al., 2018. Rotational 3D printing of damage-tolerant composites with programmable mechanics. *Proceedings of the National Academy of Sciences of the United States of America,* 115(6), pp. 1198-1203.

Saenz-Castillo, D. et al., 2019. Effect of processing parameters and void content on mechanical properties and NDI of thermoplastic composites. *Composites Part A; Applied Science and Manufacturing,* Volume 121, pp. 308-320.

Schmidt, M. et al., 2017. Laser based additive manufacturing in industry and academia. *CIRP Annals,* 66(2), pp. 561-583.

Schur, R. et al., 2021. Mechanical anisotropy and its evolution with powder reuse in Electron Beam Melting AM of Ti6Al4V. *Materials and Design,* Volume 200.

Shafighfard, T., Demir, E. & Yildiz, M., 2019. Design of fiber-reinforced variable-stiffness composites for different open-hole geometries with fiber continuity and curvature constraints. *Composite Structures,* Volume 226.

Shofner, M., Rodríguez-Macías, F., Vaidyanathan, R. & Barrera, E., 2003. Single wallnanotube and vapor grown carbonfiber reinforced polymers processed by extrusionfreeform fabrication. *Composites Part A: Applied Science annd Manufacturing,* Volume 34, pp. 1207-1217.

Somireddy, M. & Czekanski, A., 2020. Anisotropic material behavior of 3D printed composite structures – Material extrusion additive manufacturing. *Materials & Design,* Volume 195.

Soutis, C., 2020. 1- Aerospace engineering requirements in building with composites. In: P. Irving, ed. *Polymer Composites in the Aerospace Industry (Second Edition).* s.l.:Woodhead Publishing, pp. 3-22.

Su, Y., Batra, G. & Colton, J., 2020. Composite Laminate Design for Improved Open-Hole Compression Strength using Non-Standard Ply Angles and Customized Stacking Sequences Characterized by [D] Matrix. *Materials Today Communications,* Volume 24.

Tekinalp, H. et al., 2014. Highly oriented carbon fiber–polymer composites via additive manufacturing. *Composites Science and Technology,* Volume 105, pp. 144-150.

Tian, X. et al., 2017. Recycling and remanufacturing of 3D printed continuous carbon fiber reinforced PLA composites. *Journal of Cleaner Production,* Volume 142, pp. 1609-1618.

Vincent, G. et al., 2021. Characterisation and improvement of the quality of mixing of recycled thermoplastic composites. *Composites Part C: Open Access,* Volume 4.

Wang, X. et al., 2017. 3D printing of polymer matrix composites: A review and prospective. *Composites Part B: Engineering,* Volume 110, pp. 442-458.

Wheeler, D., 1990. *Tables of Screening Designs.* 2nd ed. Knoxville: SPC Press.

Wickramasinghe, S., Do, T. & Tran, P., 2020. FDM-Based 3D Printing of Polymer and Associated Composite: A Review on Mechanical Properties, Defects and Treatments. *Polymers,* 12(7).

Yap, X. et al., 2021. Mechanical properties and failure behaviour of architected alumina microlattices fabricated by stereolithography 3D printing. *International Journal of Mechanical Sciences,* Volume 196.

Yu, S., Oh, K. & Hong, S., 2019. Enhancement of the mechanical properties of basalt fiber-reinforced polyamide 6,6 composites by improving interfacial bonding strength through plasma-polymerization. *Composites Science and Technology,* Volume 182.

Zhang, D., Rudolph, N. & Woytowitz, P., 2019. *Reliable Optimized Structures with High Performance Continuous fiber thermoplastic composites from Additive Manufacturing (AM).* Charlotte, s.n.

Zhao, C., Donough, M. J., Prusty, B. G. & Xiao, J., 2021. Influences of ply wavviness and discontinuity on automated fibre placement manufactured grid stiffeners. *Composite Structures,* Volume 256.

Zhao, W. et al., 2019. Semi-empirical investigation of the interfacial shear strength of short fiber polymer composites. *Polymer Testing,* Volume 74, pp. 99-103.

Zhong, W. et al., 2001. Short fiber reinforced composites for fused deposition modeling. *Materials Science and Engineering A,* 301(2), pp. 125-130.

Zhou, Y. G., Wang, C. Y., Zhang, J. N. & Wu, H. H., 2020. Experimental and theoretical investigation on tensile properties and fracture behavoir of carbon fiber composite laminates with varied ply thickness. *Composite Structures,* Volume 249.

Ziemian, C., Sharma, M. & Ziemian, S., 2012. Anisotropic Mechanical Properties of ABS Parts Fabricated by Fused Deposition Modelling. In: M. Gokcek, ed. *Mechanical Engineering.* s.l.:InTech, pp. 159-180.